# Overmodulation Techniques of Asymmetrical Six-Phase Machine With Minimum RMS Current Ripple

Sayan Paul, *Member, IEEE*, and Kaushik Basu, *Senior Member, IEEE*

***Abstract*—An asymmetrical six-phase machine (ASPM) with two isolated neutral points is analyzed in two orthogonal subspaces: energy-transferring and harmonic subspaces. Overmodulation (OVM) techniques of ASPM extend the operating region of ASPM in the energy-transferring plane and thus attain higher voltage gain after injecting nonzero average voltage in the harmonic subspace. But due to low impedance in the harmonic subspace, the applied voltage causes large circulating current and copper loss. Hence, the RMS of the applied average voltage is minimized in the literature. It is also shown in the literature that for a given reference voltage vector in the OVM plane, there is more than one pulsewidth modulation (PWM) sequence that can achieve the minimum injection of nonzero average voltage in harmonic subspace. But they have different high-frequency ripple currents. Although the current ripple is one of the essential performance indices, its study is missing for OVM techniques of ASPM. Hence, this work studies the current ripple performances of the above PWM sequences in the OVM region. One machine parameter, which is the ratio of inductances in energy-transferring and harmonic subspaces, impacts this current ripple. The article finds the sequence with the best ripple performance for a given reference vector in the OVM region and a machine parameter. After that, a PWM technique is proposed, which improves the high-frequency current ripple RMS by 623.67% and 416.53% compared to two existing OVM techniques for a feasible machine parameter. Theoretical analysis is validated through simulation and experiments on a hardware prototype at 4.2 kW power level.**

***Index Terms*—Asymmetrical six-phase machine (ASPM), current-ripple, multiphase machines, overmodulation (OVM) technique, pulsewidth modulation (PWM).**

## I. INTRODUCTION

### A. ASPM: Advantages and Applications

AN ASYMMETRICAL six-phase machine (ASPM), also known as split-phase or dual three-phase machine, is one of the most common multiphase machines used in present days, [1], [2], [3], [4], [5]. Compared to a three-phase machine, ASPM has advantages in terms of 1) lower power rating per drive-unit; 2) higher fault-tolerance for having more number phases; and 3) lower impact of space-harmonics and excitation harmonics on air-gap flux, [5], [6], [7], [8], [9]. Hence, this machine finds applications in high-power drives, like pumps, compressors, and railway traction, and safety–critical drives, like electric vehicles, ships, and aircraft. The fault-tolerant capability of ASPM is showcased in [3], [8], [10] with postfault modeling, control, and fault-tolerant design. The electromagnetic and thermal simulation-based study of Keller et al. [9] showed that ASPM performs better than a three-phase machine in terms of maximum torque, continuous torque, efficiency, and torque pulsation for electric vehicle applications.

This article studies the pulsewidth modulation (PWM) strategy of this machine in the overmodulation (OVM) region and finds the technique with minimum high-frequency ripple current. Current ripple is inevitable in any PWM converter but must be minimized to reduce the associated copper loss and enhance drive efficiency.

### B. PWM Techniques of ASPM

A six-phase ($6\phi$) inverter fed ASPM is shown in Fig. 1. ASPM has two sets of three-phase ($3\phi$) windings, $a$, $b$, $c$ constitute one set and $a'$, $b'$, $c'$ another set, which are spatially shifted by 30°. A $6 \times 6$ transformation matrix, $T$, is proposed by [11] to model ASPM. $T$ analyses the machine in three two-dimensional (2-D) orthogonal subspaces. For an ASPM with balanced windings and two isolated neutral points, one of these 2D planes can not be excited by the $6\phi$ inverter. One 2-D plane, $\alpha - \beta$, is responsible for electromechanical energy transfer. A closed-loop speed or torque controller of ASPM demands a voltage vector be applied in the $\alpha - \beta$ or the energy-transferring plane. The equivalent circuit in the remaining plane, $z_1 - z_2$, has a lower impedance and is not associated with energy transfer. Any voltage applied in this plane results in a circulating current leading to conduction loss.

PWM techniques of ASPM synthesize the desired voltage vectors in $\alpha - \beta$ and $z_1 - z_2$ subspaces on average over a carrier cycle by applying a sequence of the switching states of $6\phi$ inverter. Note that the carrier cycle frequency is much higher than the fundamental frequency component of the line-neutral voltage. Linear modulation techniques (LMTs) of ASPM apply

Manuscript received 7 December 2023; revised 17 March 2024; accepted 25 April 2024. Date of publication 6 May 2024; date of current version 20 June 2024. This work was supported by the Department of Science and Technology, Government of India, under the project titled “Medium Voltage Grid integration of Utility Scale Renewables.” Recommended for publication by Associate Editor Jin Ye. *(Corresponding author: Sayan Paul.)*

The authors are with the Department of Electrical Engineering, Indian Institute of Science, Bangalore 560012, India (e-mail: sayanp@iisc.ac.in; kbasu@iisc.ac.in).

Color versions of one or more figures in this article are available at https://doi.org/10.1109/TPEL.2024.3397084.

Digital Object Identifier 10.1109/TPEL.2024.3397084

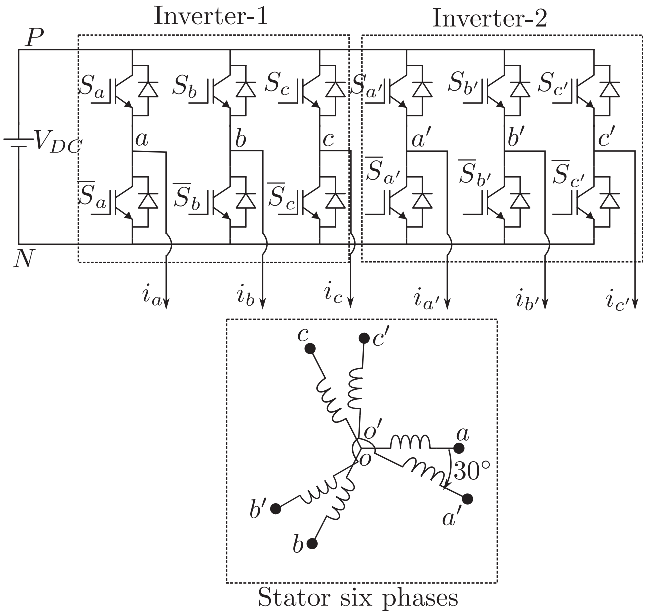

Fig. 1. Six-phase inverter fed ASPM.

zero carrier-cycle average voltage in the $z_1 - z_2$ plane, [4], [12], [13], [14], [15], [16], [17], [18], [19]. The modulation index, $M_I$, is the ratio of the peak of the fundamental frequency component of the line-neutral and dc-bus voltage. LMTs achieve $M_I$ in the range [0, 0.577].

However, a portion of the $\alpha - \beta$ plane can not be utilized by the LMTs as it requires applying nonzero average voltage in the $z_1 - z_2$ plane, [20]. This portion of the $\alpha - \beta$ plane is called the OVM region. PWM techniques, which use this region to extend the range of $M_I$ to 0.622, are known as OVM techniques. Low-frequency harmonics are injected to the average line-neutral voltage to increase inverter gain without adding any harmonics to the generated torque, [1], [2], [20], [21]. Utilization of the OVM region is desirable during high torque requirements, transient operation, and extended speed range operation, [22]. Further extension of $M_I$ from 0.622 to $\frac{2}{\pi} = 0.637$ (square wave operation) requires injection of low-frequency harmonics in $\alpha - \beta$ plane voltage, and torque, [23], [24], and hence is not considered in this article.

To limit the low-frequency harmonics in the line current for OVM operation, the magnitude of the applied average voltage vector in the $z_1 - z_2$ plane over a carrier cycle must be minimized. When the tip of the reference voltage vector in $\alpha - \beta$ lies in the OVM region, Paul and Basu [2] showed that more than one switching sequence exists that applies average voltage vectors in the $z_1 - z_2$ plane of the same minimum amplitude.

### C. Optimal PWM Techniques

As the voltages in $\alpha - \beta$ and $z_1 - z_2$ planes are realized through the application of a finite number of switching states of the six-phase inverter over a carrier cycle on an average, the inverter injects undesired voltages at the carrier frequency and its multiples leading to ripple in the line current at these frequencies and associated conduction loss. Given a restriction on the number of switching transitions of the inverter over a carrier cycle, more than one switching sequence can be applied to achieve the same average voltages. One major research direction is identifying the optimal switching sequence that minimizes the current ripple RMS for synthesizing a given average voltage vector in the $\alpha - \beta$ plane. Note that the optimal technique depends on the average voltage vector to be synthesized and on a machine parameter, $\gamma$, [4], [12]. $\gamma$ is the ratio of the equivalent leakage inductances in the two planes. A rich body of literature exists on studying the current ripples of LMTs and finding the optimal technique that minimizes the current ripple, [4], [12], [13], [14], [15], [16], [17], [18], [19]. However, to the best of the author's knowledge, no work exists on finding the optimal PWM technique in the OVM range that minimizes carrier or switching frequency ripple in the resultant line current.

### D. Contributions of this Article

Paul and Basu [2] showed that the OVM region in the $\alpha - \beta$ plane can be divided into two subregions, known as OVMZ1 and OVMZ2.

1) Given an average voltage vector in OVMZ2, this article identifies the sequence that minimizes the switching cycle RMS of the ripple current. The choice of this sequence turns out to be independent of $\gamma$ and remains the same over the entire OVMZ2 region.
2) Similarly, the optimal sequence(s) in OVMZ1 is (are) determined after comparing the current-ripple RMS values of eight possible switching sequences for a given $\gamma$.
3) Combining the above optimal sequences in OVMZ1 and OVMZ2, an optimal hybrid PWM technique is proposed that results in minimum RMS line current ripple in OVM region ($0.577 \leq M_I \leq 0.622$). A comparative study of the current ripple RMS of this technique with the existing techniques is performed. It shows significant improvement in the line-cycle RMS ripple current.
4) The article presents a carrier-based implementation of the proposed technique.

The rest of this article is organized as follows. Section II derives all the possible switching sequences in OVM; among them the optimal sequence(s) with minimum current ripple is determined in Section III. A PWM technique using the optimal sequence(s) is proposed in Section IV, and its current ripple and switching loss performances are compared with other existing techniques. The performance under different torque-speed pairs and the carrier comparison-based implementation of the proposed PWM technique are also indicated in this section. The analysis of the paper is validated through simulation and experiment in Section V. Finally, Section VI concludes this article.

## II. OVM TECHNIQUES WITH MINIMUM HARMONIC DISTORTION IN VOLTAGE

A two-level six-phase ($6\phi$) inverter-fed ASPM is shown in Fig. 1. The $6\phi$ inverter comprises two three-phase ($3\phi$) inverters, Inverter-1 and Inverter-2, connected across the same dc-bus. The

TABLE I
SWITCHING STATES OF THREE-PHASE INVERTER

| $S_a$ | $S_b$ | $S_c$ | Label | $S_a$ | $S_b$ | $S_c$ | Label |
|---|---|---|---|---|---|---|---|
| OFF | OFF | OFF | 0 | OFF | ON | ON | 4 |
| ON | OFF | OFF | 1 | OFF | OFF | ON | 5 |
| ON | ON | OFF | 2 | ON | OFF | ON | 6 |
| OFF | ON | OFF | 3 | ON | ON | ON | 7 |

ASPM has two sets of balanced star-connected $3\phi$ windings, and these windings are spatially shifted by $30°$ electrical, as shown in Fig. 1. The six terminal points, $a, b, c$, and $a', b', c'$, are directly connected to the poles of two $3\phi$ inverters and the neutral points, $o$ and $o'$, are isolated. As each $3\phi$ inverter has eight allowable switching states, the $6\phi$ inverter of Fig. 1 has 64 states. These states are labeled using an ordered pair of the form $(p, q')$, where $p$ and $q$ are the standard $3\phi$ inverter notations, as given in Table I, used to denote the switching states of Inverter-1 and Inverter-2, respectively. Therefore, $(1, 6')$ state implies top switches of the legs corresponding to phase $a$, $a'$, $c'$ and bottom switches of the legs of phase $b$, $c$, $b'$ are "ON"; other switches are "OFF."

$$\begin{bmatrix} x_\alpha \\ x_\beta \\ x_{z_1} \\ x_{z_2} \\ x_{o_1} \\ x_{o_2} \end{bmatrix} \triangleq \underbrace{\frac{1}{\sqrt{3}} \begin{bmatrix} 1 & -\frac{1}{2} & -\frac{1}{2} & \frac{\sqrt{3}}{2} & -\frac{\sqrt{3}}{2} & 0 \\ 0 & \frac{\sqrt{3}}{2} & -\frac{\sqrt{3}}{2} & \frac{1}{2} & \frac{1}{2} & -1 \\ 1 & -\frac{1}{2} & -\frac{1}{2} & -\frac{\sqrt{3}}{2} & \frac{\sqrt{3}}{2} & 0 \\ 0 & -\frac{\sqrt{3}}{2} & \frac{\sqrt{3}}{2} & \frac{1}{2} & \frac{1}{2} & -1 \\ 1 & 1 & 1 & 0 & 0 & 0 \\ 0 & 0 & 0 & 1 & 1 & 1 \end{bmatrix}}_{T} \begin{bmatrix} x_a \\ x_b \\ x_c \\ x_{a'} \\ x_{b'} \\ x_{c'} \end{bmatrix}. \tag{1}$$

Zhao and Lipo [11] proposed an orthonormal transformation matrix $T$, as given in (1), to model ASPM and the converter. $T$ transforms quantities from the original domain to three 2-D subspaces, namely, $\alpha - \beta$, $z_1 - z_2$, and $o_1 - o_2$. The detailed modeling of ASPM in [11] shows that the $\alpha - \beta$ plane is the only plane responsible for electromagnetic energy transfer. The equivalent circuits in $z_1 - z_2$ and $o_1 - o_2$ consist of winding resistance and leakage inductance. Although the latter two subspaces do not cause any torque ripple, voltage excitations in these planes result in a large circulating current due to low impedance in these planes, which subsequently cause copper loss and lower efficiency. Therefore, voltage excitations in these planes should be as minimum as possible.

$T$ is applied on the line-neutral voltages generated by 64 switching states to model the converter. It can be shown that all 64 states synthesize zero voltage-vector in $o_1 - o_2$ plane, and therefore, discussion of this plane is excluded in subsequent sections. The voltage vectors in $\alpha - \beta$ and $z_1 - z_2$ subspaces of these 64 states are given in [11]. The voltage vectors in $\alpha - \beta$ divide the whole plane into 24 equivalent sectors, among which one sector, conventionally called sector-1, is our region of interest. Fig. 2 shows the mapping of 16 states whose voltage vectors in the $\alpha - \beta$ plane are adjacent to sector-1. As indicated in Fig. 2(a), the sector numbers are surrounded by oval-shaped curves. $z$ denotes the zero-states of $3\phi$ inverter in Fig. 2, i.e., $z \in \{0, 7\}$. Therefore, these 16 states result in 9 distinct nonzero voltage vectors and one zero-vector in $\alpha - \beta$ and $z_1 - z_2$ subspaces.

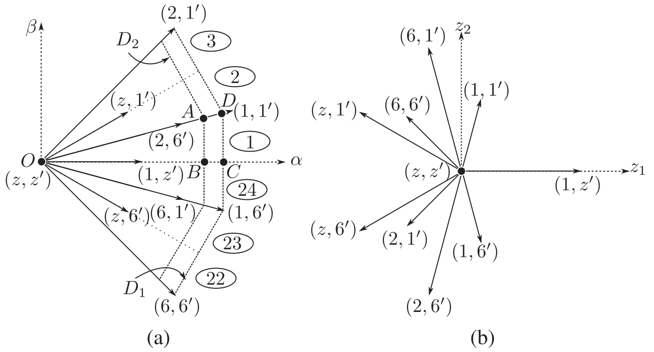

Fig. 2. Mapping of 16 states adjacent to sector-1. (a) $\alpha - \beta$. (b) $z_1 - z_2$.

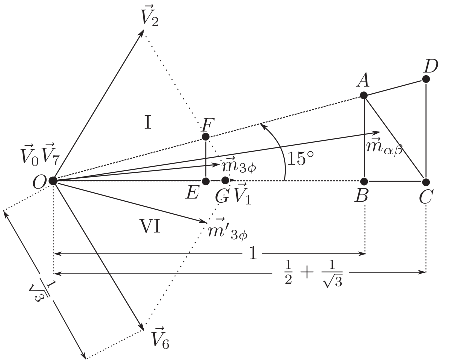

Fig. 3. $\vec{m}_{\alpha\beta}$ in sector-1 OVM region and corresponding $\vec{m}_{3\phi}$ and $\vec{m}'_{3\phi}$.

The reference voltage vector in $\alpha - \beta$, $\vec{V_{ref}} \overset{\Delta}{=} \bar{v}_\alpha + j\bar{v}_\beta$, can lie in one of the two regions–1) Linear region-where the average voltage injection in $z_1 - z_2$ plane can be made zero, i.e., $\bar{v}_{z_1} + j\bar{v}_{z_2} = 0$; 2) OVM region- to synthesize $\vec{V_{\text{ref}}}$ in this region, $\bar{v}_{z_1} + j\bar{v}_{z_2}$ can not be made zero. Here, the bar over a variable represents the carrier-cycle average of that variable. Two do-decagons, $D_1$, and $D_2$, are partially shown in Fig. 2(a), which encompass the six sectors shown in the figure. The region within the inner do-decagon, $D_2$, is the linear region. The inscribed area between do-decagons $D_1$ and $D_2$ represent the OVM region, [2], [20]. It can be seen from Fig. 2(a) that any sector other than 1 and 24 is either equivalent to 1 (odd sectors) or 24 (even sectors). Even sector-24 is mirror symmetric to sector-1 with respect to the $\alpha$-axis. Therefore, the discussion will be restricted to sector-1. The linear and OVM region of sector-1, triangle $OAB$ ($\Delta OAB$) and the quadrilateral $ABCD$ ($\square ABCD$), are shown separately in Fig. 3. The lengths of the voltage vectors and reference vectors are normalized with respect to dc-bus voltage, $V_{\text{DC}}$, in Fig. 3 and these normalized reference vectors in $\alpha - \beta$ and $z_1 - z_2$ planes are denoted by $\vec{m}_{\alpha\beta} \overset{\Delta}{=} m_\alpha + jm_\beta$ and $\vec{m}_{z_1 z_2} \overset{\Delta}{=} m_{z_1} + jm_{z_2}$, respectively, where $m_x = \frac{\bar{v}_x}{V_{\text{DC}}}, x \in \{\alpha, \beta, z_1, z_2\}$. This paper studies the high-frequency current-ripple performances of PWM techniques in the OVM region of sector-1, i.e., $\vec{m}_{\alpha\beta} \in \square ABCD$.

Several PWM techniques exist for the OVM operation of ASPM, [1], [2], [20], [21], where each of these techniques injects different average voltages in $z_1 - z_2$ plane for a given $\vec{m}_{\alpha\beta}$. This article considers $\vec{m}_{z_1z_2}$ as given in [1], [2], which gives minimized $|\vec{m}_{z_1z_2}|$ in every switching cycle. Henceforth, the RMS of the injected low-frequency harmonic voltage over a line cycle will be minimized. Based on the solution, OVM region, $\square ABCD$, is divided into two zones- $\Delta BAC$, denoted by OVM Zone-1 (OVMZ1); and $\Delta ACD$, denoted by OVM Zone-2 (OVMZ2). For a given $\vec{m}_{\alpha\beta} \in \square ABCD$, the optimal $\vec{m}_{z_1z_2}$ in OVMZ1 and OVMZ2 is given as follows (see[2]):

$$\vec{m}_{z_1z_2} = \begin{cases} 0; & I_1 \le 0; I_2 \le 0 \quad \text{(Linear)} \\ I_1; & I_1 > 0; I_2 \le 0 \quad \text{(OVMZ1)} \\ I_1 + jI_2; & I_1 > 0, I_2 > 0 \quad \text{(OVMZ2)} \end{cases}$$

$$I_1 : m_\alpha - 1; \qquad I_2 : \left(2\sqrt{3}m_\alpha + m_\beta - (2+\sqrt{3})\right). \tag{2}$$

Let us define $3\phi - 2\phi$ Clarke's transformation, as given in (3). When this transformation is applied on the line-neutral voltages generated by the eight switching states of $3\phi$ inverters, Inverter-1 and Inverter-2, we get the corresponding $3\phi$ voltage space vectors. Fig. 3 shows the nonzero vectors of states 1, 2, and 6 of Table I; and zero-vector of states 0 and 7. Here, $\vec{V}_x$ denotes the voltage-vector of $x$th switching state of $3\phi$ inverter, and $x \in \{0, 1 \ldots 7\}$. When (3) is applied on the average line-neutral voltages of $3\phi$ inverters ($\overline{v}_{xo}$ for Inverter-1 and $\overline{v}_{x'o'}$ for Inverter-2), the reference voltage vectors of two inverters are obtained. Here, where $x \in \{a, b, c\}$. These $3\phi$ reference vectors are normalized with respect to dc-bus voltage, $V_{\mathrm{DC}}$, and are denoted by $\vec{m}_{3\phi}$ (for Inverter-1) and $\vec{m'}_{3\phi}$ (for Inverter-2). The relationships between $3\phi$ reference vectors and $\vec{m}_{\alpha\beta}, \vec{m}_{z_1z_2}$ are derived in [20], which are given in (4). Here, $*$ denotes the complex conjugate of the vector

$$\vec{x}_{3\phi} = \frac{1}{\sqrt{3}}\left(\left(x_a - \frac{x_b}{2} - \frac{x_c}{2}\right) + j\frac{\sqrt{3}}{2}(x_b - x_c)\right) \tag{3}$$

$$\vec{m}_{3\phi} = \frac{1}{2}\left(\vec{m}_{\alpha\beta} + \vec{m}^{*}_{z_1z_2}\right); \quad \vec{m'}_{3\phi} = \frac{1}{2}\left(\vec{m}_{\alpha\beta} - \vec{m}^{*}_{z_1z_2}\right)e^{-j30^\circ}. \tag{4}$$

The rest of this section discusses about the systematic procedure to derive all possible sequences of switching states and their dwell times in the OVM region. The subsequent sections find the technique with minimum RMS value of high-frequency current-ripple.

### *A. Determine Vector-Sets Per $3\phi$ Inverter and Their Corresponding Duty-Ratios*

Determination of all possible sequences of ASPM in the OVM region is equivalent to finding possible ways to synthesize $\vec{m}_{3\phi}$ and $\vec{m'}_{3\phi}$ in per $3\phi$ inverter basis. For the given $\vec{m}_{\alpha\beta} \in \square ABCD$ and the corresponding $\vec{m}_{z_1z_2}$, as given in (2), one can determine $\vec{m}_{3\phi}$ and $\vec{m'}_{3\phi}$ after applying (4). With this operation, the followings three observations can be made about the positions of $\vec{m}_{3\phi}$ and $\vec{m'}_{3\phi}$, as concluded in [2]

1) For any $\vec{m}_{\alpha\beta}$ within $\square ABCD$, $\vec{m'}_{3\phi}$ lies on the line joining the tips of $\vec{V}_1$ and $\vec{V}_6$, as indicated in Fig. 3.
2) When $\vec{m}_{\alpha\beta} \in \Delta BAC$, $\vec{m}_{3\phi}$ lies within $\Delta EFG$, where $OE = \frac{OB}{2}$, Fig. 3.
3) When $\vec{m}_{\alpha\beta} \in \Delta ACD$, $\vec{m}_{3\phi}$ lies on the line $FG$, where $FG$ is part of the hexagonal boundary joining the tips of $\vec{V}_1$ and $\vec{V}_2$, Fig. 3.

To synthesize the above $\vec{m'}_{3\phi}$, the only choice Inverter-2 has to apply the set of switching states $\{1', 6'\}$. Here, the states of Inverter-2 are labeled by primes. Similarly, when $\vec{m}_{3\phi}$ lies on the line $FG$, Inverter-1 applies the set $\{1, 2\}$. But, if $\vec{m}_{3\phi}$ lies within $\Delta EFG$, Inverter-1 needs to apply at least three distinct vectors. Two common choices for selecting the set of three distinct vectors are– 1) nearest two active vectors and one zero vector, 2) nearest three active vectors. Therefore, Inverter-1 applies $\{z, 1, 2\}$ or $\{6, 1, 2\}$ set of states in order to synthesize $\vec{m}_{3\phi} \in \Delta EFG$, where $z \in \{0, 7\}$.

Once the set of vectors are decided, the dwell-times of application of these vectors can be decided after solving a set of equations. For example, dwell-times of states $z$, 1 and 2, $d_z$, $d_1$, and $d_2$, respectively, can be found by solving

$$d_1\vec{V}_1 + d_2\vec{V}_2 + d_z 0 = \vec{m}_{3\phi}; \quad d_1 + d_2 + d_z = 1. \tag{5}$$

Substituting $\vec{m}_{3\phi}$ from (4) and $\vec{m}_{z_1z_2}$ from (2), $d_z$, $d_1$, and $d_2$ can be expressed as functions of $m_\alpha$ and $m_\beta$ and these functions are shown in the first subtable under Table II. Similarly, one can find the duty ratios of other possible sets to synthesize $\vec{m}_{3\phi}$ and $\vec{m'}_{3\phi}$ and these duty expressions are given in Tables II (for OVMZ1) and III (for OVMZ2). It is possible to show that the duty ratios of these sets always lie within the range [0,1] while $\vec{m}_{\alpha\beta} \in \square ABCD$, therefore, implementation is feasible.

### *B. Determine the Sequences of $3\phi$ Inverters Corresponding to Each Vector-Set*

As given below, two rules, *R1* and *R2*, are followed during the sequence design of $3\phi$ inverters from the given vector-set.

*R1*. Each semiconductor device is allowed to turn ON and OFF a maximum of once over a carrier cycle.

*R2*. The switching sequence will be mirror-symmetric along carrier half-period, $\frac{T_s}{2}$.

*R1* is imposed to avoid multiple switching of a leg within a carrier-cycle, $T_s$, and increase in instantaneous switching frequency, [13]. All the vectors within a vector-set need to be applied at least once within $\frac{T_s}{2}$ to satisfy *R2*. PWM techniques, which follow both *R1* and *R2*, can be implemented after comparing the duty signals with the triangular carrier. It is possible to show that all the switching sequences of vector-set $\{z, 1, 2\}$, which follow the above two rules, can be of the form $0-1-2-7-2-1-0$ within $T_s$ or $0-1-2-7$ within $\frac{T_s}{2}$. We will only consider the vector sequence within $\frac{T_s}{2}$ as the other half mirrors symmetric. Similarly, $\{6, 1, 2\}$, $\{1, 2\}$ and $\{1', 6'\}$ sets have the sequences like $6-1-2, 1-2$ and $1'-6'$, respectively.

### *C. Sequence Grouping of $6\phi$ Inverter*

As the synthesis of $\vec{m}_{3\phi}$ and $\vec{m'}_{3\phi}$ of (4) ensures the application of the desired $\vec{m}_{\alpha\beta}$ and $\vec{m}_{z_1z_2}$, Inverter-1 can apply one of the two possible sequences, $0-1-2-7$ or $6-1-$

TABLE II
DUTY RATIOS OF SWITCHING STATES OF INVERTER-1 AND INVERTER-2 FOR $\vec{m}_{\alpha\beta} \in \Delta BAC$ (OVMZ1)

| | Set $\{z, 1, 2\}$ (Inverter-1) |
|---|---|
| d1 | $\sqrt{3}m_\alpha - \frac{1}{2}m_\beta - \frac{\sqrt{3}}{2}$ |
| d2 | $m_\beta$ |
| dz | $(1 + \frac{\sqrt{3}}{2}) - \sqrt{3}m_\alpha - \frac{1}{2}m_\beta$ |

| | Set $\{6, 1, 2\}$ (Inverter-1) |
|---|---|
| d1 | $2\sqrt{3}m_\alpha - (1 + \sqrt{3})$ |
| d2 | $(1 + \frac{\sqrt{3}}{2}) - \sqrt{3}m_\alpha + \frac{1}{2}m_\beta$ |
| d6 | $(1 + \frac{\sqrt{3}}{2}) - \sqrt{3}m_\alpha - \frac{1}{2}m_\beta$ |

| | Set $\{1', 6'\}$ (Inverter-2) |
|---|---|
| d1′ | $\frac{1}{2} + \frac{\sqrt{3}}{2}m_\beta$ |
| d6′ | $\frac{1}{2} - \frac{\sqrt{3}}{2}m_\beta$ |

TABLE III
DUTY RATIOS OF SWITCHING STATES OF INVERTER-1 AND INVERTER-2 FOR $\vec{m}_{\alpha\beta} \in \Delta ACD$ (OVMZ2)

| | Set $\{1, 2\}$ (Inverter-1) |
|---|---|
| d1 | $2\sqrt{3}m_\alpha - (1 + \sqrt{3})$ |
| d2 | $(2 + \sqrt{3}) - 2\sqrt{3}m_\alpha$ |

| | Set $\{1', 6'\}$ (Inverter-2) |
|---|---|
| d1′ | $3m_\alpha + \sqrt{3}m_\beta - (1 + \sqrt{3})$ |
| d6′ | $(2 + \sqrt{3}) - 3m_\alpha - \sqrt{3}m_\beta$ |

2, when $\vec{m}_{\alpha\beta} \in \Delta BAC$ and sequence $1 - 2$ when $\vec{m}_{\alpha\beta} \in \Delta ACD$. Inverter-2, whereas, applies sequence $1' - 6'$ throughout $\square ABCD$. Therefore, $2 \times 1 = 2$ different combinations of $3\phi$ sequences can occur in OVMZ1, and only one combination is possible in OVMZ2. Each of these combinations can be arranged in two ways by changing the relative position of one $3\phi$ sequence to another. Therefore, a total of four arrangements or sequence groups are possible in OVMZ1 (labeled as S1 to S4), and two sequence groups (S5 and S6) are possible in OVMZ2, as shown in Table IV.

The current-ripple performance of OVM techniques is the subject of study in this article. Zero-vector splitting affects the current-ripple, as we know from the $3\phi$ inverter literature, [25], [26], [27]. Therefore, the zero-vector dwell-times are split between the redundant zero states, 0 and 7, of Inverter-1, as shown in Table IV. The distribution factors of S1 and S2 sequences are denoted by $y$ and $x$, respectively, Table IV. Note, S3, S4, S5, and S6 sequences were already derived in [2]. For the sequence-groups S1 and S2 in OVMZ1, [2] considered three discrete values of $y$ and $x$,. viz, $x, y \in \{0, \frac{1}{2}, 1\}$, leading to $2 \times 3 = 6$ distinct sequences from these two groups. Here, a continuum between 0 and 1 is considered as $x$ and $y$ to study the effect of the distribution factor on the ripple performance of ASPM.

The average switching frequency is kept the same when comparing current-ripple performances of different PWM techniques. Therefore, the factor $k_f$ is introduced here, defined as the ratio of the total number of switching (combining turn-ON and turn-OFF) over $T_s$ and the total number of legs (6 in this case). One should note that if $x = 0$ or $x = 1$, one of the legs of Inverter-1 does not switch over one $T_s$. Same is true when $y = 0$ or $y = 1$. Therefore, $k_f$ is a function of $x$ (for S2) or $y$ (for S1), which is shown in the last column of Table IV.

### *D. Determine the Vector Sequence and Corresponding Duty Ratios of $6\phi$ Inverter*

To evaluate the current ripples in both $\alpha - \beta$ and $z_1 - z_2$ planes, one needs to know the sequence of application of $6\phi$ switching states and their dwell times. From the given sequence groups, as above, one can find these from the position of $\vec{m}_{\alpha\beta}$ and the choice of $x$ or $y$. For example, in case of sequence-group S1, Inverter-1 and Inverter-2 have used $\{z, 1, 2\}$ and $\{1', 6'\}$, respectively. The duty ratios of these states are given in the first and third subtables of Table II from where it is possible to show that $d6' \geq d2 + dz$ and $d1' \geq d6'$ for $\vec{m}_{\alpha\beta} \in \Delta BAC$. Therefore, the arrangement shown in Table IV is the only possible way to occur in S1. From this arrangement, one can easily determine the $6\phi$ sequence by looking at the top and bottom rows of the arrangements, which in this case is $(0, 1') - (1, 1') - (1, 6') - (2, 6') - (7, 6')$. The dwell times of these states and the sequence are indicated in the fourth column of Table IV. Similarly, the possible arrangements, corresponding sequences, and dwell times of $6\phi$ switching states for other sequence groups are also given in Table IV. One should notice here that the dwell times involved in 1) S1 and S2 should be referred from the first and third sub-tables of Table II; 2) S3 and S4 should be referred from the second and third sub-tables of Table II, 3) S5 and S6 should be referred from Table III.

The $6\phi$ states of Table IV can be referred from Fig. 2 from where it can be seen that the nonzero vectors in $\alpha - \beta$ are of three different lengths- large (denoted by L), medium (M) and small (S). For example, S1 with $y = 0$ applies two large vectors, $(1, 1')$ and $(1, 6')$, one medium vector, $(2, 6')$, and one small vector, $(7, 6')$, in $\alpha - \beta$ plane. 2L+1M+1S denotes the type of vectors used here. The types of vectors of other sequences are also mentioned in the fifth column of Table IV.

## III. DETERMINATION OF OPTIMAL SEQUENCE(S) WITH MINIMUM CURRENT RIPPLE

This section compares the carrier-cycle RMS ripple current of the sequences derived in the previous section. For S1 and S2, the effect of $y$ and $x$ on the ripple current are also studied, where $0 \leq x, y \leq 1$. The ripple currents in both $\alpha - \beta$ and $z_1 - z_2$ subspaces are caused due to the error voltages between the instantaneously applied voltages and the average voltages, termed as ripple voltage, in the respective subspaces. Note this ripple current is different from the low-frequency current of harmonic order 5th, 7th, $12\,m \pm 5, m = 0, 1, 2\ldots$ flowing in $z_1 - z_2$ subspace due to application of nonzero $\vec{m}_{z_1z_2}$ of (2), [2]. The ripple voltage contains the switching frequency and its multiple harmonic components along with their side-bands. These ripple voltages cause the ripple currents to flow through the equivalent circuits of the respective subspaces, which are predominantly inductive in nature at this frequency range. Let, the inductances seen by $\alpha - \beta$ and $z_1 - z_2$ planes are denoted by $L_{\alpha\beta}$, and $L_{z_1z_2}$, respectively. The RMS ripple current over

TABLE IV
SEQUENCE-GROUPS AND 6$\phi$ SEQUENCES IN OVMZ1 AND OVMZ2

| Zone | Case | Sequence-group | 6$\phi$ sequence over $\frac{T_s}{2}$ | Type of vectors | $k_f$ |
|---|---|---|---|---|---|
| OVMZ1 | S1 | $\overbrace{0}^{yd_z}$ \| 1 \| 2 \| $\overbrace{7}^{(1-y)d_z}$<br>$1'$ \| $6'$ | $\underbrace{(0,1')}_{yd_z}-\underbrace{(1,1')}_{d1'-yd_z}-\underbrace{(1,6')}_{d1+yd_z-d1'}-\underbrace{(2,6')}_{d2}-\underbrace{(7,6')}_{(1-y)d_z}$ | 2L+1M+1S; $y\in\{0,1\}$<br>2L+1M+2S; $O.W.$ | $\frac{1}{2}; y,x\in\{0,1\}$<br>$\frac{2}{3}; O.W.$ |
| | S2 | $\overbrace{0}^{xd_z}$ \| 1 \| 2 \| $\overbrace{7}^{(1-x)d_z}$<br>$6'$ \| $1'$ | $\underbrace{(0,6')}_{xd_z}-\underbrace{(1,6')}_{d6'-xd_z}-\underbrace{(1,1')}_{d1+xd_z-d6'}-\underbrace{(2,1')}_{d2}-\underbrace{(7,1')}_{(1-x)d_z}$ | 3L+1S; $x\in\{0,1\}$<br>3L+2S; $O.W.$ | |
| | S3 | 6 \| 1 \| 2<br>$1'$ \| $6'$ | $\underbrace{(6,1')}_{d6}-\underbrace{(1,1')}_{d1'-d6}-\underbrace{(1,6')}_{d6'-d2}-\underbrace{(2,6')}_{d2}$ | 2L+2M | $\frac{1}{2}$ |
| | S4 | 6 \| 1 \| 2<br>$6'$ \| $1'$ | $\underbrace{(6,6')}_{d6}-\underbrace{(1,6')}_{d6'-d6}-\underbrace{(1,1')}_{d1'-d2}-\underbrace{(2,1')}_{d2}$ | 4L | |
| OVMZ2 | S5 | 1 \| 2<br>$1'$ \| $6'$ | $\underbrace{(1,1')}_{d1'}-\underbrace{(1,6')}_{d6'-d2}-\underbrace{(2,6')}_{d2}$ | 2L+1M | $\frac{1}{3}$ |
| | S6 | 1 \| 2<br>$6'$ \| $1'$ | $\underbrace{(1,6')}_{d6'}-\underbrace{(1,1')}_{d1'-d2}-\underbrace{(2,1')}_{d2}$ | 3L | |

a carrier-cycle combining all six phases, $\tilde{i}_{\mathrm{RMS}}$, for an OVM technique is given as

$$\begin{aligned}\tilde{i}^2_{\mathrm{RMS}} &= k_f^2\left(\tilde{\lambda}^2_{\alpha\beta}(m_\alpha,m_\beta)+\gamma^2\tilde{\lambda}^2_{z_1z_2}(m_\alpha,m_\beta)\right)\\ &= \tilde{i}^2_{\alpha\beta,\mathrm{RMS}}(m_\alpha,m_\beta)+\tilde{i}^2_{z_1z_2,\mathrm{RMS}}(m_\alpha,m_\beta)\end{aligned}\qquad(6)$$

where, $\tilde{i}_{\alpha\beta,\mathrm{RMS}}=k_f\tilde{\lambda}_{\alpha\beta}$, and $\tilde{i}_{z_1z_2,\mathrm{RMS}}=k_f\gamma\tilde{\lambda}_{z_1z_2}$. These $\tilde{i}_{\alpha\beta}$ and $\tilde{i}_{z_1z_2}$ are the switching-cycle current ripple RMS values in $\alpha-\beta$ and $z_1-z_2$ planes, respectively. The derivation of the above expression is given in [12] for linear techniques. Compared to linear PWM techniques of ASPM, one needs to consider the nonzero $\vec{m}_{z_1z_2}$, as given in (2), for OVM techniques. In (6), $\tilde{i}_{\alpha\beta,\mathrm{RMS}}$, $\tilde{i}_{z_1z_2,\mathrm{RMS}}$, and $\tilde{i}_{\mathrm{RMS}}$ are per-unitized with respect to base current $\frac{V_{\mathrm{DC}}T_{\mathrm{sw}}}{L_{\alpha\beta}}$. The factor $k_f \overset{\Delta}{=} \frac{T_s}{T_{\mathrm{sw}}}$ depends upon the sequence and $x$ or $y$ value, as discussed earlier, and is introduced here to compare different techniques keeping average switching frequency, $F_{\mathrm{sw}} \overset{\Delta}{=} \frac{1}{T_{\mathrm{sw}}}$, same. $\gamma \overset{\Delta}{=} \frac{L_{\alpha\beta}}{L_{z_1z_2}}$ is machine dependent parameter, which is the ratio of $L_{\alpha\beta}$ and $L_{z_1z_2}$. The study in [28] showed that $\gamma$ depends upon the winding pitch factor and the geometry of the slot of the machine. Full-pitch winding has the lowest $\gamma$ value, whereas $\frac{5}{6}$-th pitch factor winding has the maximum $\gamma$. Based on the $\gamma$ values reported in the literature, [12], [17], [28], this article considers 1.5 to 10 as the practical range of $\gamma$, which is same as the range considered in [4]. $\tilde{\lambda}_{\alpha\beta}$ and $\tilde{\lambda}_{z_1z_2}$ are RMS flux ripples in the two planes, and they are functions of both $\vec{m}_{\alpha\beta}$ and $\vec{m}_{z_1z_2}$ in OVM. However, $\vec{m}_{z_1z_2}$ can be written as functions of $m_\alpha$ and $m_\beta$, as shown in (2). Therefore, these ripple fluxes can be expressed as sole functions of $m_\alpha$ and $m_\beta$, as (6).

The optimal sequence(s) in OVMZ1 is determined after comparing the $\tilde{i}_{\mathrm{RMS}}$, calculated using (6), for the given $\vec{m}_{\alpha\beta}\in\Delta BAC$ and $\gamma$. For S1 and S2, $y$ and $x$ are varied between 0 and 1 with a step of 0.01 to find the optimal value, $y^*$ and $x^*$, such that $\tilde{i}_{\mathrm{RMS}}$ is minimum among all possible values between 0 and 1. The corresponding $\tilde{i}_{\mathrm{RMS}}$ values are denoted by $\tilde{i}_{\mathrm{RMS}}(y^*)|_{S1}$ (for S1) and $\tilde{i}_{\mathrm{RMS}}(x^*)|_{S2}$ (for S2). Fig. 4 shows the flowchart of determining the optimal $x^*$ and the corresponding $\tilde{i}_{\mathrm{RMS}}(x^*)|_{S2}$ for S2 sequence group. The $\tilde{i}_{\mathrm{RMS}}$ of S3 and S4 sequences, denoted by $\tilde{i}_{\mathrm{RMS}}|_{S3}$ and $\tilde{i}_{\mathrm{RMS}}|_{S4}$, are also determined using (6). After that, the best sequence and the minimum current ripple, $\tilde{i}^*_{\mathrm{RMS}}$, for the given $\vec{m}_{\alpha\beta}$ in OVMZ1 are determined after finding the minimum from the below set as

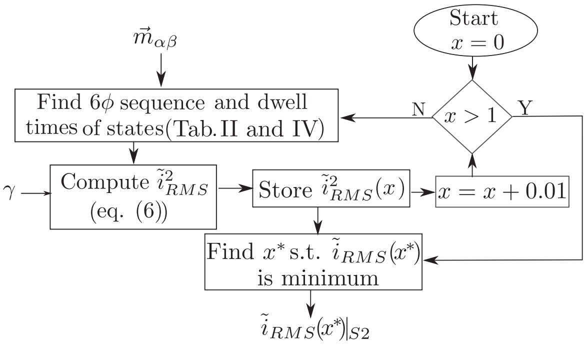

Fig. 4. Algorithm to find the $x^*$ and $\tilde{i}_{\mathrm{RMS}}(x^*)$ for the sequence group S2.

$$\tilde{i}^*_{\mathrm{RMS}}=\min\{\tilde{i}_{\mathrm{RMS}}(y^*)|_{S1},\tilde{i}_{\mathrm{RMS}}(x^*)|_{S2},\tilde{i}_{\mathrm{RMS}}|_{S3},\tilde{i}_{\mathrm{RMS}}|_{S4}\}.$$

The same procedure is followed for all possible $\vec{m}_{\alpha\beta}$ in OVMZ1 ($\Delta BAC$). Similarly, the best sequence among S5 and S6 in OVMZ2 is found for $\vec{m}_{\alpha\beta}\in\Delta ACD$ and given $\gamma$. Fig. 5 shows these optimal sequences and the corresponding dwell-time distribution factor in the entire OVM region for $\gamma=2$ and 6. The key observations of this study are as follows.

1) Two sequences show the optimality in OVMZ1 for the entire feasible range of $\gamma$, as seen from Fig. 5(a). These are-i) S4 (4 L); ii) S2 with $x=1$ (i.e., $x^*=1$), labeled as S2$|_{x=1}$. When $x=1$, the dwell time state $(7,1')$ in the second row of Table IV becomes zero. Hence, the applied sequence by S2$|_{x=1}$ technique is $(0,6')-(1,6')-(1,1')-(2,1')$ and the vector type is (3L+1S).
2) S4 shows optimality in the whole $\Delta BAC$ for $\gamma>3.75$, as can be seen from Fig. 5(b).

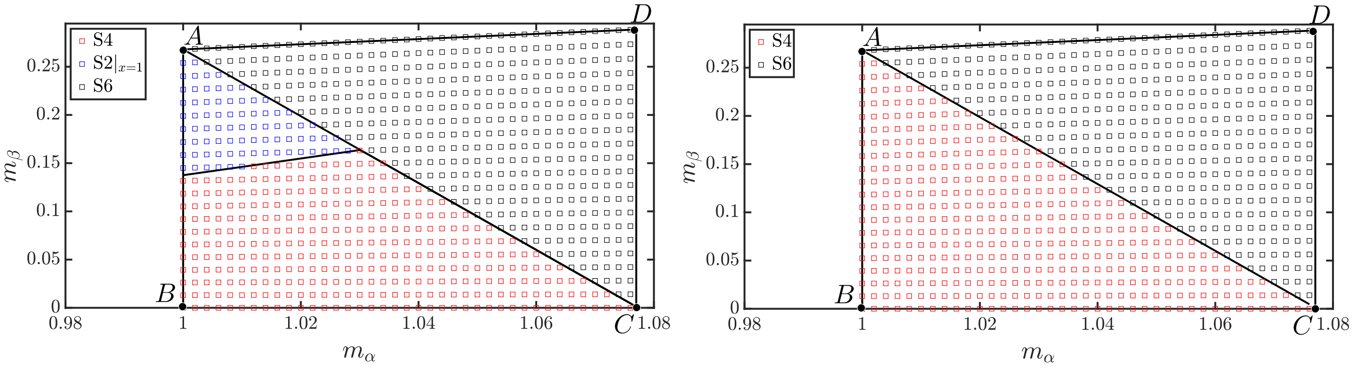

(a) (b)

Fig. 5. Region-wise optimal techniques for two different $\gamma$ values. (a) $\gamma = 2$. (b) $\gamma = 6$.

3) In OVMZ2 or $\Delta ACD$, S6 is the only optimal sequence irrespective of the value of $\gamma$.
4) Both S4 and $S2|_{x=1}$ result in S6 when the dwell-times $d6$ (of S4) and $dz$ (of $S2|_{x=1}$) become zero.

One can follow the two steps adopted by this article to find the optimal sequence for other multiphase machine with different phase number – 1) finding all possible switching sequences, 2) comparing current ripples, combining all subspaces, of these sequences using an analytical expression similar to (6). The ripple current analysis of a machine with phase number seven or higher requires to analyse more than one harmonic subspace along with $\alpha - \beta$. Although analysis of five-phase machine involves $\alpha - \beta$ and $z_1 - z_2$, direct extension of ASPM techniques to five-phase machine is not possible primarily because of two reasons- 1) six-phase inverter has more number of switching states or degrees of freedom (64 states) compared to five-phase inverter (32 states); 2) the orientation of the space-vectors in $\alpha - \beta$ and $z_1 - z_2$ planes, which impacts the current ripple performance, are different for five-phase and six-phase converters. The ripple current analysis of this article can also be extended to an ASPM whose two sets of three-phase windings are driven from two independent voltage sources of equal dc magnitude.

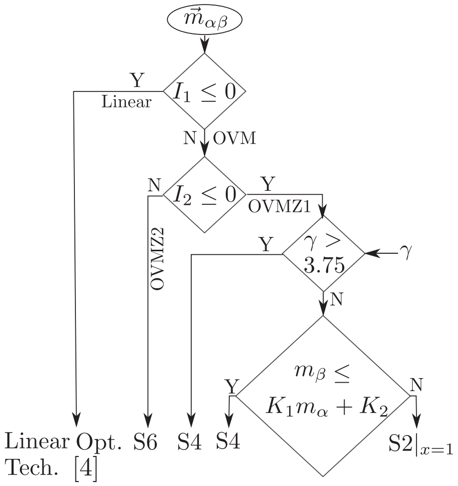

Fig. 6. Flowchart shows the choice of the sequences of the proposed technique in sector-1.

## IV. PROPOSED OPTIMAL PWM TECHNIQUE AND ITS COMPARISON WITH EXISTING TECHNIQUES

This article proposes implementing the optimal sequence in every carrier cycle based on the position of $\vec{m}_{\alpha\beta}$ so that the line-cycle ripple RMS can be minimized. The optimal technique of [4] is adopted in the linear region. When the tip of $\vec{m}_{\alpha\beta}$ is in OVMZ2, S6 is the only sequence to be applied irrespective of the value of $\gamma$, as discussed in the previous section. Similarly, S4 is the optimal sequence throughout OVMZ1 for $\gamma > 3.75$. But, when $\vec{m}_{\alpha\beta}$ is in OVMZ1 and $\gamma \leq 3.75$, one should apply either S4 or $S2|_{x=1}$ based on $(\tilde{i}_{\mathrm{RMS}})_{S4} \lesseqgtr (\tilde{i}_{\mathrm{RMS}})_{S2|_{x=1}}$. In order to compare $\tilde{i}_{\mathrm{RMS}}$ of S4 and $S2|_{x=1}$ for different values of $\gamma$, the analytical closed-form expressions of $k_f^2 \tilde{\lambda}_{\alpha\beta}^2$ and $k_f^2 \tilde{\lambda}_{z_1 z_2}^2$ of (6) are first derived. These are fifth order polynomials of two variables, $m_\alpha$ and $m_\beta$, which are not given here for the brevity. Evaluation of these polynomials online in real-time processor for comparing $(\tilde{i}_{\mathrm{RMS}})_{S4}$ and $(\tilde{i}_{\mathrm{RMS}})_{S2|_{x=1}}$ becomes computationally heavy. Hence, this calculation-intensive process is simplified applying Taylor's series approximation which results a linear inequality, of the form $m_\beta \lesseqgtr K_1 m_\alpha + K_2$, to be checked. Here, $K_1$ and $K_2$ are functions of $\gamma$, which are given in (7). As the machine parameter, $\gamma$, does not change in run-time, the calculation of (7) needs be done offline once. Fig. 6 shows the choice of the optimal sequences in different regions of operation of ASPM in a flowchart format. The expressions of $I_1$ and $I_2$ are given in (2)

$$K_1(\gamma) = \frac{1}{-0.045\gamma^3 + 0.329\gamma^2 - 0.392\gamma + 0.998}$$

$$K_2(\gamma) = \frac{1}{0.083\gamma^3 - 0.756\gamma^2 + 1.204\gamma - 1.439}. \quad (7)$$

The following two sections compare the current ripple performance and the switching loss of the proposed technique with the existing techniques. Two techniques, adopted by [1] and [2], are selected for comparison purposes. These techniques also implement the same average $z_1 - z_2$ voltages, as defined in (2), in the OVM region. Note the other OVM techniques of [20], [21], [23] do not apply the minimum RMS voltage in the $z_1 - z_2$ plane, as given in (2), causing more circulating current and higher low-frequency harmonic distortion. As the applied switching sequences and the corresponding ripple currents are strong functions of the average injected voltage, techniques with a different average voltage are not compared here. The first technique, [1], uses S3 (2L+2 M) in OVMZ1, and S5 (2L+1 M) in OVMZ2 (refer Table IV). Although [2] derived eight sequences in OVMZ1 and two sequences in OVMZ2, but it used S1 with $y = \frac{1}{2}$ resulting 2L+1M+2S in OVMZ1, and S5 (2L+1 M) in OVMZ2 for the hardware implementation. This strategy is the second technique for comparison. As mentioned earlier, all the derived sequences of [2] were included in Section III for the current ripple study.

Let us define the modulation index, $M_I$, as the ratio of the peak of the fundamental frequency component present in the line-neutral voltage and dc-bus voltage, $V_{\text{DC}}$. It can be shown that sinusoidal voltages in the $\alpha - \beta$ plane during steady-state operation results in $\vec{m}_{\alpha\beta} = \sqrt{3}M_I e^{j\omega_o t}$, where $\omega_o$ is the fundamental frequency in rad/s. The complete range of $M_I$, i.e., $M_I \in [0, 0.622]$, for which the circular $\vec{m}_{\alpha\beta}$ always lies within do-decagon $D_1$ of Fig. 2(a), is divided in three ranges, as

1) For $0 \leq M_I \leq 0.577$, $\vec{m}_{\alpha\beta}$ remains always within the linear region, [4].
2) For $0.577 < M_I \leq 0.597$, $\vec{m}_{\alpha\beta}$ resides in either linear ($I_1 \leq 0$) or OVMZ1 ($I_1 > 0$), [2], as shown in Fig. 6.
3) For $0.597 < M_I \leq 0.622$, $I_1$ is always greater than zero. $\vec{m}_{\alpha\beta}$ lies in either OVMZ1 ($I_2 \leq 0$) or OVMZ2 ($I_2 > 0$), [2], shown in Fig. 6.

The expressions of $I_1$ and $I_2$ for sector-1 are given in (2). For a fair comparison, the same modulation strategy, as given in [4], is adopted in the linear region of operation for all three compared techniques. Therefore, their performances will be the same in $0 \leq M_I \leq 0.577$, hence, not shown in this paper. As this article is about minimizing the current ripple in the OVM region, all the performance comparisons between the proposed technique and the existing techniques are performed in the range of $0.577 \leq M_I \leq 0.622$, i.e., in the OVM region.

### A. Comparison of Current Ripple Performance

For a given $\gamma$ and the sequence, the carrier-cycle ripple RMS combining all six phases, $\tilde{i}_{\text{RMS}}$, depends upon the position of $\vec{m}_{\alpha\beta}$, (6). With $\vec{m}_{\alpha\beta} = \sqrt{3}M_I e^{j\omega_o t}$, the line-cycle ripple RMS of each phase, $\tilde{I}_{\text{RMS}}$, in steady-state can be obtained by integrating $\tilde{i}_{\text{RMS}}$, which is now a function of $M_I$ and $\omega_o t$, over $\omega_o t = 0$ to $\omega_o t = 2\pi$ and dividing this integral by 6, as (8). Here, the division by six is done to get per-phase ripple RMS. Substituting $\tilde{i}_{\text{RMS}}$ from (6), (8) further splits $\tilde{I}_{\text{RMS}}$ into two components, $\tilde{I}_{\alpha\beta,\text{RMS}}$ and $\tilde{I}_{z_1 z_2,\text{RMS}}$, to show the ripple contributions by $\alpha - \beta$ and $z_1 - z_2$ planes individually

$$\begin{aligned}\tilde{I}^2_{\text{RMS}}(M_I) &= \frac{1}{6}\left(\frac{1}{2\pi}\int_0^{2\pi}\tilde{i}^2_{\text{RMS}}(M_I,\omega_o t)\,d(\omega_o t)\right)\\ &= \underbrace{\frac{1}{12\pi}\int_0^{2\pi}\tilde{i}^2_{\alpha\beta,\text{RMS}}\,d(\omega_o t)}_{\tilde{I}^2_{\alpha\beta,\text{RMS}}(M_I)} + \underbrace{\frac{1}{12\pi}\int_0^{2\pi}\tilde{i}^2_{z_1 z_2,\text{RMS}}\,d(\omega_o t)}_{\tilde{I}^2_{z_1 z_2,\text{RMS}}(M_I)}.\end{aligned} \tag{8}$$

TABLE V
MAXIMUM PERCENTAGE IMPROVEMENT SHOWN BY THE PROPOSED TECHNIQUE COMPARED TO [1], [2]

| $\gamma$ | Improvement to [1] | Improvement to [2] |
|---|---|---|
| 2 | 140.01 ($M_I = 0.597$) | 259.23 ($M_I = 0.597$) |
| 6 | 369.92 ($M_I = 0.594$) | 569.59 ($M_I = 0.597$) |
| 10 | 416.53 (at $M_I = 0.592$) | 623.67 ($M_I = 0.597$) |

Fig. 7(a) and (b) compares the carrier cycle ripple current trajectories of the proposed technique with the two techniques of [1] and [2] in $\alpha - \beta$ and $z_1 - z_2$ planes, respectively, at $M_I = 0.597$, $\omega_o t = 14.5^\circ$ and for $\gamma = 2$. The same comparison for $\gamma = 6$ are shown in Fig. 7(c) and (d). For the same value of $\vec{m}_{\alpha\beta}$ ($M_I = 0.597$ and $\omega_o t = 14.5^\circ$), the ripple current contribution of $z_1 - z_2$ plane becomes more significant as $\gamma$ value increases, whereas the contribution of $\alpha - \beta$ plane remains almost unchanged. The analytical line-cycle ripple RMS in these two subspaces are compared in Fig. 7(e) and (f) for $M_I \in [0.577, 0.622]$ and at three discrete values of $\gamma$, i.e., $\gamma = 2, 6, 10$. Total line-cycle ripple RMS, $\tilde{I}_{\text{RMS}}$, combining the contributions of $\tilde{I}_{\alpha\beta,\text{RMS}}$ and $\tilde{I}_{z_1 z_2,\text{RMS}}$ as given in (8), are compared in Fig. 7(g)–(i), respectively, for these three $\gamma$ values. The line plots are the analytical plots and the asterisk marks are the simulated data points which will be referred later. For a fair comparison, all these techniques adopt the optimal linear technique of [4] in the linear region, and hence, all of them have the same RMS values at $M_I = 0.577$. As $M_I$ increases from 0.577, the differences of $\tilde{I}_{\text{RMS}}$ values between the proposed technique and the two existing techniques first increase up to $M_I = 0.597$ and then gradually reduce. Although the $\tilde{I}_{\alpha\beta,\text{RMS}}$ of the proposed optimal method is worse than the existing two techniques for all three $\gamma$ values, $\tilde{I}_{z_1 z_2,\text{RMS}}$ of the proposed technique is far better than the existing techniques, resulting in the proposed method to have the minimum total ripple RMS current, $\tilde{I}_{\text{RMS}}$. Comparing the scales of ordinate axis of Fig. 7(e) and (f), it can be concluded that as $\gamma$ increases, the contribution of $\tilde{I}_{z_1 z_2,\text{RMS}}$ in $\tilde{I}_{\text{RMS}}$ becomes more predominant.

The maximum percentage improvements due to the proposed technique compared to [1] and [2] at $\gamma = 2, 6, 10$ values are tabulated in Table V. The $M_I$ values at which they occur are also indicated in the bracket. Note the proposed technique significantly improves ripple RMS current (as high as 416% and 623%) compared to the existing techniques within the feasible range of $\gamma$. This improvement results in a considerable reduction in copper loss due to ripple currents and enhancement of efficiency, specifically for medium-voltage fed high-power drives, where the base current is high for higher $V_{\text{DC}}$ and lower $F_{\text{sw}}$. One such example is given in the Appendix.

### B. Comparison of Switching Loss

For a constant dc-link voltage and average switching frequency, the normalised switching loss of $x$th leg over a switching cycle, $P_x|_{T_{\text{sw}}}$, can be evaluated using (9), [29]. Here, $n_x$ is the number of switching transitions (one turn-ON and turn-OFFresults in one transition) of $x$th leg over a subcycle; $|i_x|$ is the magnitude of the current flowing through the leg; and $I_{pk}$ is

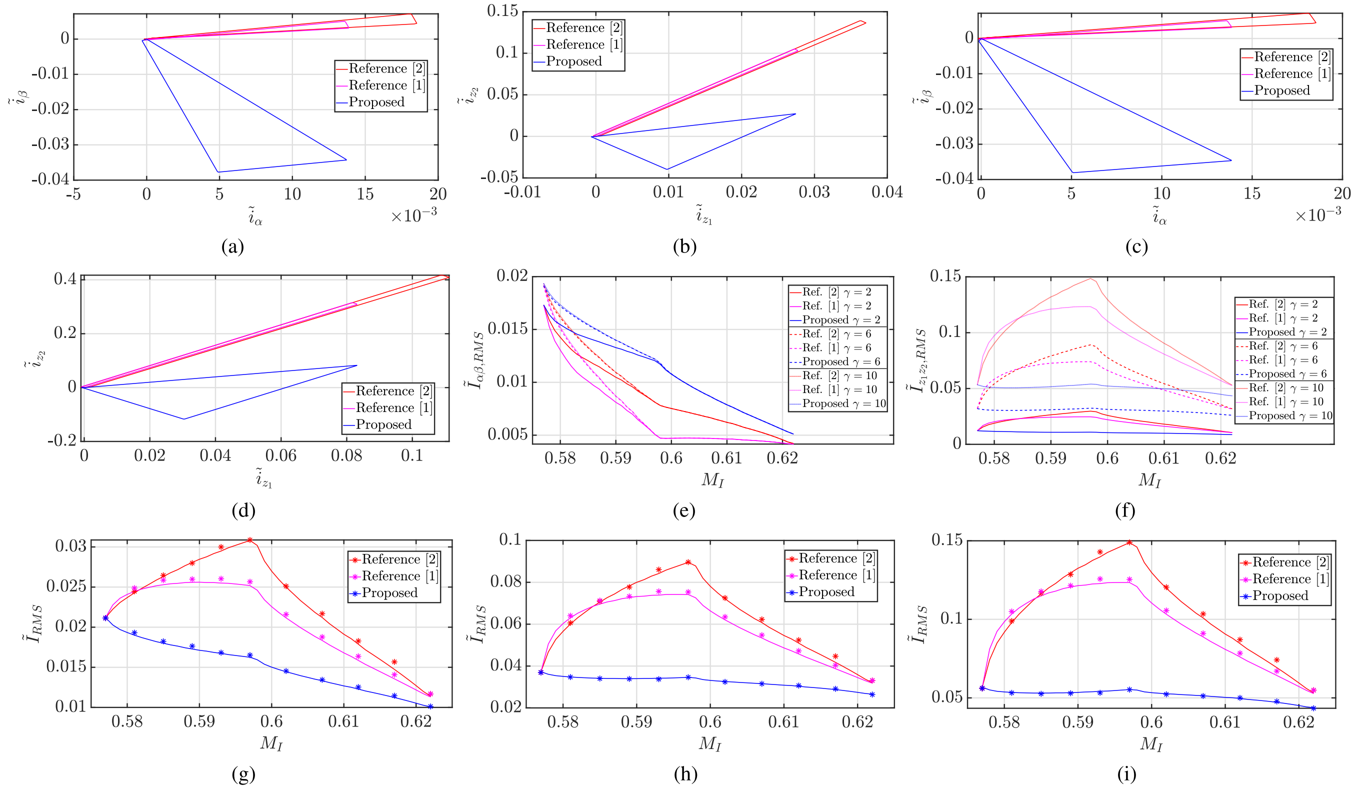

(a) (b) (c)

(d) (e) (f)

(g) (h) (i)

Fig. 7. Comparison of ripple currents of three techniques (base current is $\frac{V_{DC}T_{sw}}{L_{\alpha\beta}}$). (a) $\tilde{i}_\alpha$, $\tilde{i}_\beta$ at $\gamma = 2$ ($M_I = 0.597$, $\omega_o t = 14.5°$). (b) $\tilde{i}_{z_1}$, $\tilde{i}_{z_2}$ at $\gamma = 2$ ($M_I = 0.597$, $\omega_o t = 14.5°$). (c) $\tilde{i}_\alpha$, $\tilde{i}_\beta$ at $\gamma = 6$ ($M_I = 0.597$, $\omega_o t = 14.5°$). (d) $\tilde{i}_{z_1}$, $\tilde{i}_{z_2}$ at $\gamma = 6$ ($M_I = 0.597$, $\omega_o t = 14.5°$). (e) $\tilde{I}_{\alpha\beta,\mathrm{RMS}}$ vs. $M_I$. (f) $\tilde{I}_{z_1 z_2,\mathrm{RMS}}$ vs. $M_I$. (g) $\tilde{I}_{\mathrm{RMS}}$ vs. $M_I$ at $\gamma = 2$. (h) $\tilde{I}_{\mathrm{RMS}}$ vs. $M_I$ at $\gamma = 6$. (i) $\tilde{I}_{\mathrm{RMS}}$ vs. $M_I$ at $\gamma = 10$.

the peak of the fundamental current. Two practical assumptions are taken in this formulation – 1) the magnitudes of the harmonic current flowing due to OVM operation are much smaller compared to the fundamental current, therefore, its contribution toward switching loss is negligible; 2) effect of high-frequency ripple current in the switching loss is neglected

$$P_{x,T_{\mathrm{sw}}} = \frac{n_x|i_x|}{I_{pk}}\frac{1}{k_f} \tag{9}$$

$$P_{T_{\mathrm{sw}}} = \sum_{x=a,b,c}^{a',b',c'} P_{x,T_{\mathrm{sw}}}. \tag{10}$$

The total power loss over a switching cycle combining all six legs, $P_{T_{\mathrm{sw}}}$, is given by (10). As $k_f$ and $n_x$ are different for different optimal sequences in three regions (linear, OVMZ1, and OVMZ2) and the proposed technique adopts these optimal sequences based on the position of steady-state $\vec{m}_{\alpha\beta} = \sqrt{3}M_I e^{j\omega_o t}$, $P_{T_{\mathrm{sw}}}$ is function of $M_I$ and $\omega_o t$. This reference voltage vector causes current vector $\sqrt{3}I_{pk}e^{j(\omega_o t-\phi)}$ to flow in the $\alpha - \beta$ plane, where $\phi$ is the load power-factor angle. As $i_x$ in (9) involves $\phi$, $P_{T_{\mathrm{sw}}}$ is also function of $\phi$. Hence, $P_{T_{\mathrm{sw}}} = P_{T_{\mathrm{sw}}}(M_I, \omega_o t, \phi)$. The switching power loss over the line cycle combining all six legs is obtained after integrating $P_{T_{\mathrm{sw}}}$ over $\omega_o t = 0$ to $\omega_o t = 2\pi$, as given (11). If all the 12 switches undergo one transition (turn-ON and turn-OFF) in each switching cycle, this loss becomes independent of power-factor and its value is $\frac{12}{\pi}$, [29], [30]. Henceforth, this loss is per-unitized with respect to $\frac{12}{\pi}$ in (11) and denoted by $P_{\mathrm{sw}}$

$$P_{\mathrm{sw}}(M_I, \phi) = \frac{\pi}{12}\left(\frac{1}{2\pi}\int_0^{2\pi} P_{T_{\mathrm{sw}}}(M_I, \omega_o t, \phi)d(\omega_o t)\right). \tag{11}$$

Fig. 8 compares $P_{\mathrm{sw}}$ Versus $M_I$ of the proposed technique and the two existing techniques for $\gamma = 2, 6$ at 0.9 lagging power factor, which is common for the motors. The proposed method and the technique of [1] have lower switching loss compared to that of [2] for $0.577 \leq M_I \leq 0.622$ and for all $\gamma$ values within feasible range. For $\gamma > 3.75$, both the proposed technique and [1] have same $P_{\mathrm{sw}}$ for all power factors. For $\gamma \leq 3.75$, where the proposed optimal method uses both S4 and $\mathrm{S2}|_{x=1}$ techniques in OVMZ1 region, $P_{\mathrm{sw}}$ of the proposed method is slightly higher ($< 8.5\%$) than [1] method for a small range of $M_I$, but same for the remaining $M_I$ values. These observations remain true for any lagging power factor greater than 0.75.

### *C. Performance for Different Torque–Speed Pairs*

The performance indices of different PWM techniques are shown as function of $M_I$ in the above two subsections. One can relate the steady-sate electromagnetic torque, $T_e$, and the speed of the machine, $\omega_r$, with $M_I$ through (12) for an induction

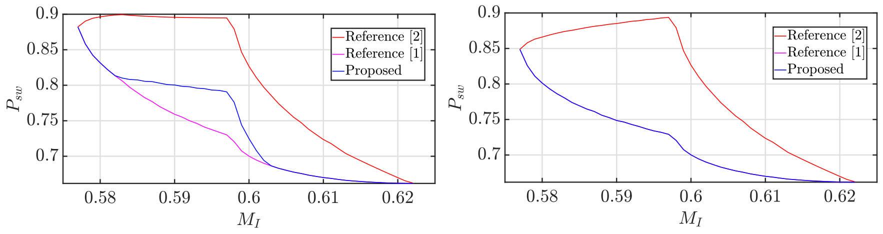

(a) (b)

Fig. 8. Comparison of $P_{\text{sw}}$ Versus $M_I$ for 0.9 lagging power factor. (a) $\gamma = 2$. (b) $\gamma = 6$.

TABLE VI
PER-PHASE EQUIVALENT CIRCUIT PARAMETERS OF ASPM

| | |
|---|---|
| Stator and rotor resistances (50 Hz), $r_s$ & $r'_r$ | 0.675 Ω |
| Magnetizing inductance (50 Hz), $L_M$ | 0.186 H |
| Stator and rotor leakage inductances (50 Hz), $L_{ls}$ & $L'_{lr}$ | 3.75 mH |
| High-frequency $\alpha - \beta$ plane inductance, $L_{\alpha\beta}$ | 4 mH |
| High-frequency $z_1 - z_2$ plane inductance, $L_{z_1 z_2}$ | 2.35 mH |
| Ratio of inductances in $\alpha - \beta$ and $z_1 - z_2$, $\gamma$ | 1.69 |

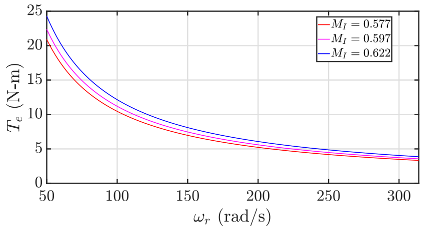

Fig. 9. Torque speed pairs with same $M_I$ value.

machine. Here, $s$ is the slip. Other parameters are labeled in Table VI. For deriving (12), the mechanical output power is equated with the electrical power delivered by the steady-state equivalent circuit of ASPM (magnetizing inductance is neglected)

$$T_e \times \omega_r \approx \frac{6\left(\frac{M_I V_{\text{DC}}}{\sqrt{2}}\right)^2 r'_r s(1-s)}{(sr_s + r'_r)^2 + s^2\omega_o^2(L_{ls} + L'_{lr})^2}. \tag{12}$$

It is clear from (12) that for the same slip, $s$, more than one pair of $(T_e, \omega_r)$ result into same $M_I$, hence, same $\tilde{I}_{\text{RMS}}$ and $P_{\text{sw}}$. With $V_{\text{DC}} = 270$ V (as used in the experiment) and 1% slip, Fig. 9 shows three sets of $(T_e, \omega_r)$ pairs for which $M_I$ values remain constant and they correspond to three $M_I$ values,. viz, 0.577, 0.597, and 0.622. Similarly, for other $(T_e, \omega_r)$ pairs, one can find $M_I$ from (12) and determine $\tilde{I}_{\text{RMS}}$ and $P_{\text{sw}}$ from the given analysis of this article.

### *D. Carrier-Comparison-Based Implementation in sector-1*

From the given $\vec{m}_{\alpha\beta}$, the proposed OVM technique can be implemented in sector-1 following the three steps given as follows.

1) Step-1: Determine the optimal sequence using the algorithm of Fig. 6. For $\gamma > 3.75$, this step does not need any extra computation to implement the proposed method compared to other two existing methods. If $\gamma \leq 3.75$, one needs to evaluate the linear inequality, $m_\beta \leq K_1 m_\alpha + K_2$, which needs additional 1 multiplication, 1 summation, and 1 comparison compared to other existing methods.

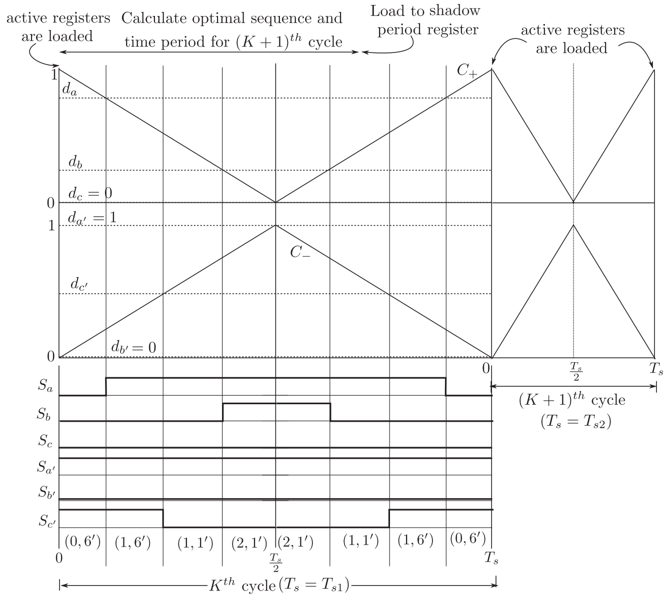

Fig. 10. Figure shows carrier-based implementation of $\text{S2}|_{x=1}$ in sector-1 ($K$th cycle) and change of carrier frequency from $K$th to $(K+1)$th cycle.

2) Step-2: Determine the duty-ratios of top switches of six legs for a particular sequence using the expressions given in Tables II and III. For example, Inverter-1 applies sequence $0 - 1 - 2$ to synthesize $\text{S2}|_{x=1}$ in OVMZ1. For this sequence, the duty ratios of the top switches of $a$, $b$, and $c$ legs, denoted by $d_a$, $d_b$, and $d_c$, are as follows, where $d_1$ and $d_2$ are replaced from the first subtable of Table II

$$d_a = d_1 + d_2; \qquad d_b = d_2; \qquad d_c = 0.$$

3) Step-3: Generate the gating signals of the top switches of six legs after comparing duty signals with one of the two 180° phase-shifted triangular carriers, $C_+$ or $C_-$, which vary linearly from 0 to 1, [31], [32]. The gating signals of the bottom switches are obtained after complementing the gating-signals of the top switches and incorporating dead-time to it. Fig. 10 shows these

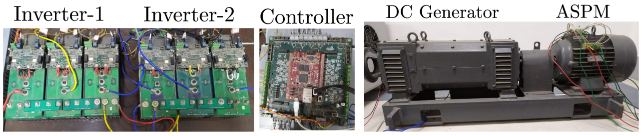

(a) (b)

Fig. 11. Experimental set-up. (a) Six-phase inverter and controller. (b) ASPM coupled with dc generator.

TABLE VII
FUNDAMENTAL, 5TH AND 7TH HARMONICS OF $v_{ab}$ OF FIG. 12(C) AND (F) (IN V)

| $M_I$ | Fundamental | | Fifth Harmonic | | Seventh Harmonic | |
|---|---|---|---|---|---|---|
| | Anal. | Expt. | Anal. | Expt. | Anal. | Expt. |
| 0.589 | 280.55 | 278.5 | 2.52 | 2.32 | 2.29 | 2.08 |
| 0.612 | 291.50 | 287.59 | 19.77 | 19.57 | 2.76 | 2.66 |

two carriers and the comparison of duty signals with these carriers to obtain $S2|_{x=1}$ sequence in sector-1, i.e., $(0,6') - (1,6') - (1,1') - (2,1') - (1,1') - (1,6') - (0,6')$ over $T_s$. Here, $d_j$ and $S_j$ are the duty-ratio and the corresponding gating-signal of the top switch of $j$th-leg.

Similar procedure is followed to implement all the optimal OVM sequences in t24 sectors.

## V. SIMULATION AND EXPERIMENTAL VALIDATION

The proposed strategy is verified through simulation in MATLAB Simulink and experiment on a 5 kW, two poles asymmetrical six-phase induction motor coupled with dc generator load. SKM75GB123D IGBT-based two $3\phi$ inverters and Zynq-7010-based controller card are used to drive the machine. The experimental setup is shown in Fig. 11. The per-phase machine parameters at 50 Hz and the inductance values in $\alpha - \beta$ and $z_1 - z_2$ planes at high-frequency (near to switching frequency) are mentioned in Table VI. The $\gamma$ of this machine with full-pitched winding is 1.69. During experiments and simulations, $V_{\text{DC}} = 275$ V and $F_{\text{sw}} = 5$ kHz are maintained. Based on the value of $k_f$, the carrier frequency, $F_s \overset{\Delta}{=} \frac{F_{\text{sw}}}{k_f}$, is changed from one sequence to another. Fig. 10 elaborates the change of $F_s$ in two consecutive carrier cycles with time-periods $T_{s1}$ and $T_{s2}$. The time period of the optimal sequence to be implemented in the next cycle is written in the shadow period register. This period along with other duty values will be loaded from shadow register to the active register at the beginning of the next carrier cycle, as indicated in Fig. 10. For example, EPwmxRegs.TBPRD register is used to write the period for TI-28379D processor. To enable the shadowing of period, PRDLD bits of TBCTL registers are used. The instant of loading from the shadow register to the the active register can be set using PRDLDSYNC bits of TBCTL2 register. Similar concept of shadow and active registers are used to implement the carrier with variable time-period in FPGA-based controller.

### A. *Verification of Fundamental Operation, Low-Frequency Total Harmonic Distortion (THD), and the Correctness of the Implementation*

The fundamental operation of the proposed optimal strategy is validated through experiments at 11 discrete $M_I$ values as $M_I \in \{ 0.577, 0.581, 0.585, 0.589, 0.593, 0.597, 0.602, 0.607, 0.612, 0.617, 0.622 \}$. The machine is driven at constant V/f so that at $M_I = 0.622$, the output line-neutral fundamental voltage is 120 V RMS; the output frequency is 50 Hz, and the power is 4.2 kW. The experimental results are shown in Fig. 12 for $M_I = 0.589$ and $M_I = 0.612$, each belongs to the two different $M_I$ ranges of OVM operation, as discussed in Section IV.

The four-phase currents $(i_a, i_b, i_{a'}, i_{b'})$, line–line voltage $(v_{ab})$, and the spectrum of line–line voltage corresponding to $M_I = 0.589$ are shown in Fig. 12(a)–(c), respectively. Similar results for $M_I = 0.612$ are shown in Fig. 12(d)–(f), respectively. The phase currents in both cases have lower order harmonics (5th, 7th, 17th, 19th, $12\,m \pm 5, m = 0, 1, 2..$) due to the injection of harmonic voltage in the $z_1 - z_2$ plane for OVM operation. Table VII tabulates the analytical values and the experimental values, obtained from the spectra of Fig. 12(c) and (f), of the fundamental, 5th and 7th harmonic components present in $v_{ab}$. The experimental values are close to the analytical values. The THD due to these applied low-frequency harmonic components (harmonics up to 3.5 kHz) is evaluated for all of the operating $M_I$ values from both experimental and simulated data points and compared with analytical values in Fig. 12(g). The solid line in Fig. 12(g) shows the analytical THD corresponding to optimal harmonic voltage injection, as given by [2]. And, experimental and simulated values are indicated by red and black asterisk marks, respectively, in Fig. 12(g). The close agreement between the analytical and experimentally obtained THD confirms that the implemented technique results in minimum low-frequency harmonic injection in the $z_1 - z_2$ plane. The fundamental operation is further verified from-1) 30° phase-shifted pairs with respect to fundamental frequency, $\{i_a, i_{a'}\}$, $\{i_b, i_{b'}\}$; 2) 120° phase-shifted currents, $\{i_a, i_b\}$, $\{i_{a'}, i_{b'}\}$.

It is known that the applied low-frequency harmonics in OVM appear only in $z_1 - z_2$ plane and hence do not create any low-frequency torque ripple. Currents in $\alpha - \beta$ plane corresponding to phase currents of Fig. 12(a) and (d) are shown in Fig. 12(h) and (i), respectively, to validate the above claim. To obtain the currents in $\alpha - \beta$ and $z_1 - z_2$ planes, the four-phase currents, suppose $i_a$, $i_b$, $i_{a'}$, and $i_{b'}$, are recorded in a. csv file from the scope. As $i_c = -i_a - i_b$ and $i_{c'} = -i_{a'} - i_{b'}$, $i_c$ and $i_{c'}$ can be found from these four currents. After that, transformation $T$, (1), is applied on these phase currents. The $i_\alpha$ and $i_\beta$ in Fig. 12(h) and (i) are balanced sinusoid, devoid of low-frequency harmonics, and phase-shifted by 90°. The generated torque is associated with only $\alpha - \beta$ subspace, [11].

The correctness of the implemented optimal sequences is also verified. Fig. 13(a)–(c) shows the pole-voltage waveforms, $v_{xN}$, over a carrier-cycle of $S2|_{x=1}$, S4, and S6 sequences in sector-1. The values of $(M_I, \omega_o t)$ for the $\vec{m}_{\alpha\beta} = \sqrt{3} M_I e^{j\omega_o t}$, at which these sequences are captured, are $(0.589, 12^\circ)$, $(0.589, 3^\circ)$, and $(0.612, 12^\circ)$, respectively. The switching sequences mentioned in the figures can be derived from these pole voltage waveforms, which are the same as expected.

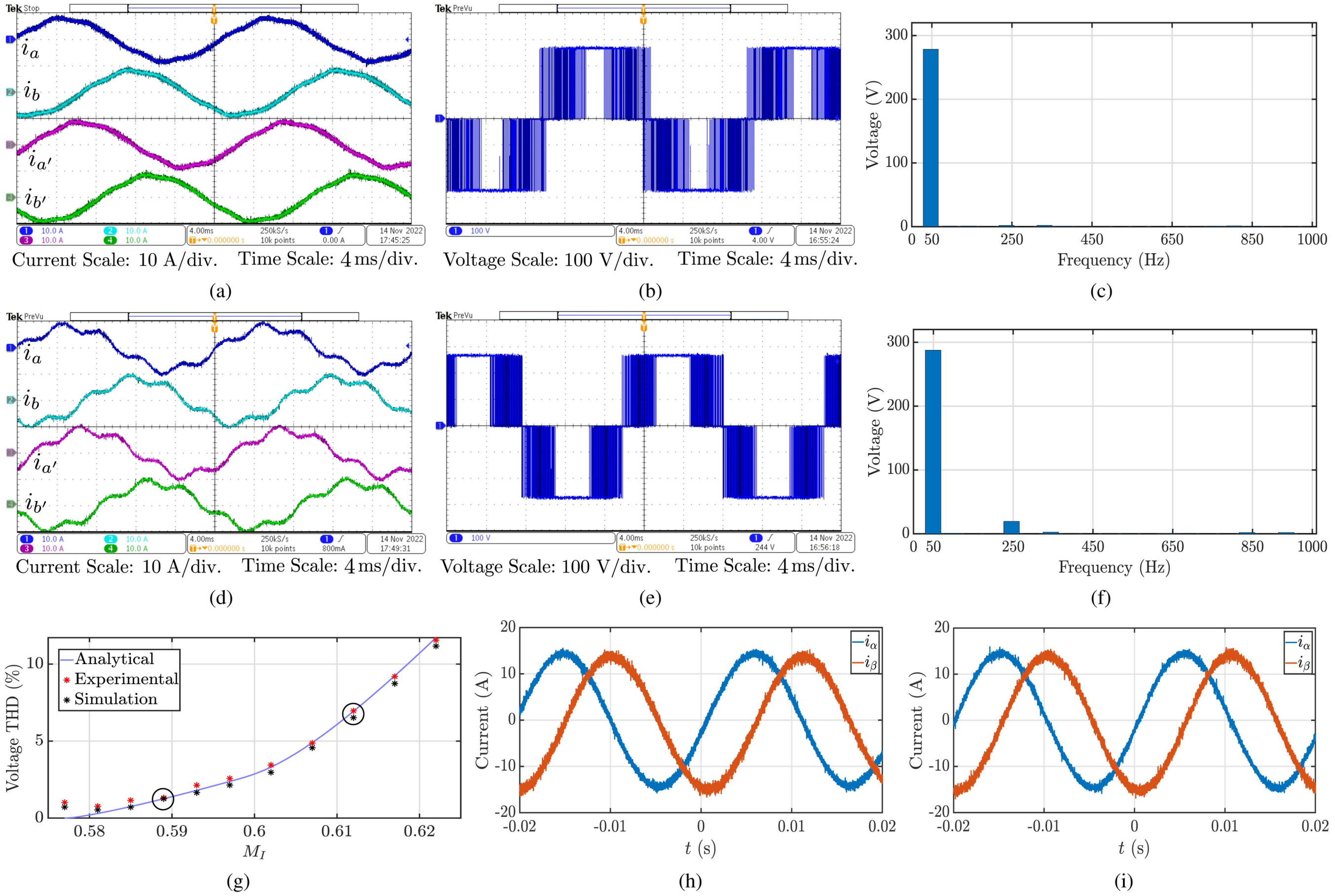

Fig. 12. Experimental results to verify the fundamental operation and low-frequency THD of the proposed OVM technique. (a) $i_a, i_b, i_{a'}$, and $i_{b'}$ at $M_I = 0.589$. (b) $v_{ab}$ at $M_I = 0.589$. (c) Spectrum of $v_{ab}$ at $M_I = 0.589$. (d) $i_a, i_b, i_{a'}$, and $i_{b'}$ at $M_I = 0.612$. (e) $v_{ab}$ at $M_I = 0.612$. (f) Spectrum of $v_{ab}$ at $M_I = 0.612$. (g) Analytical (solid line), simulated (black asterisk), and experimental (red asterisk) voltage THD versus $M_I$ plots. (h) $i_\alpha, i_\beta$ of Fig. 12(a). (i) $i_\alpha, i_\beta$ of Fig. 12(d).

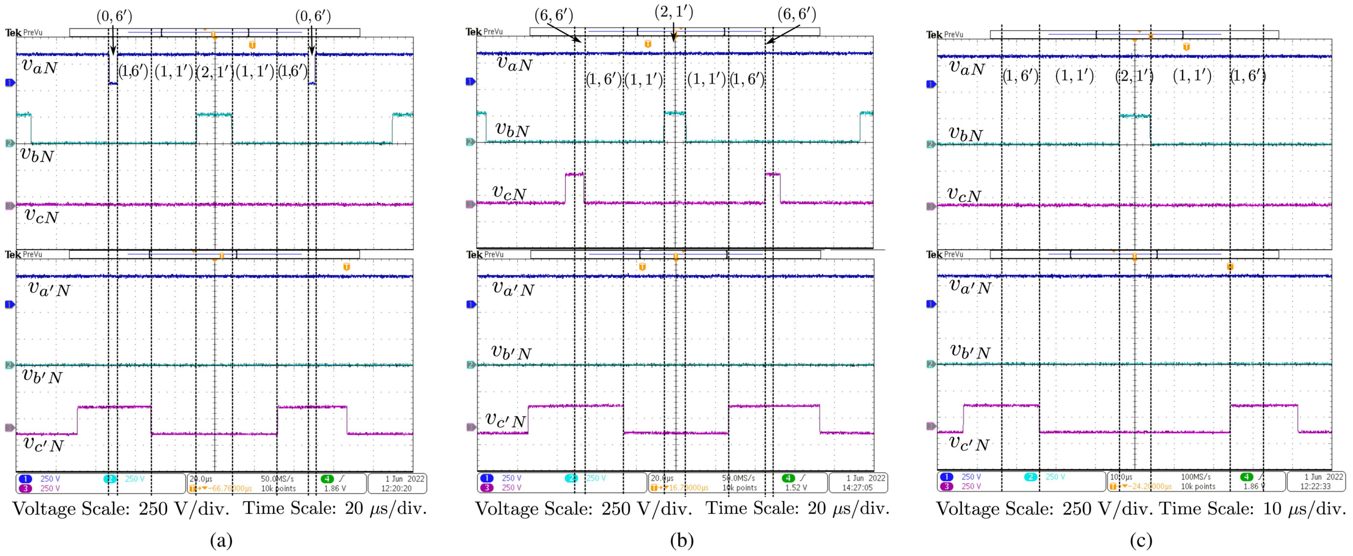

Fig. 13. Experimental results to validate the correctness of implementation of the proposed technique. (a) Sequence $\mathrm{S2}|_{x=1}$ at $M_I = 0.589, \omega_o t = 12^\circ$. (b) Sequence S4 at $M_I = 0.589, \omega_o t = 3^\circ$. (c) Sequence S6 at $M_I = 0.612, \omega_o t = 12^\circ$.

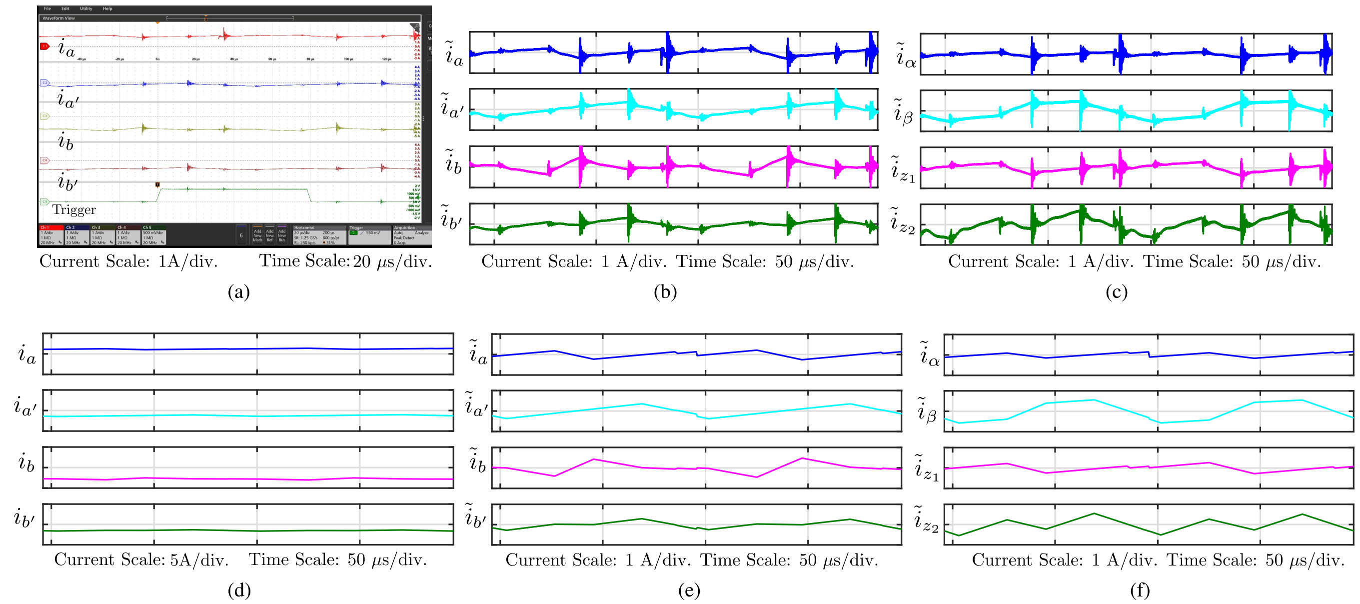

Fig. 14. Experimental and simulated carrier cycle ripple currents following the proposed technique at $M_I = 0.597$ and $\omega_o t = 10°$. (a) Experimental $i_a, i_b, i_{a'}, i_{b'}$. (b) Experimental $\tilde{i}_a, \tilde{i}_b, \tilde{i}_{a'}, \tilde{i}_{b'}$. (c) Experimental $\tilde{i}_\alpha, \tilde{i}_\beta, \tilde{i}_{z_1}, \tilde{i}_{z_2}$. (d) Simulated $i_a, i_b, i_{a'}, i_{b'}$. (e) Simulated $\tilde{i}_a, \tilde{i}_b, \tilde{i}_{a'}, \tilde{i}_{b'}$. (f) Simulated $\tilde{i}_\alpha, \tilde{i}_\beta, \tilde{i}_{z_1}, \tilde{i}_{z_2}$.

### *B. Verification of the Current-Ripple Performance*

To show the experimental result of carrier-cycle current ripple of the proposed technique, four phase currents, $i_a, i_{a'}, i_b, i_{b'}$, over one carrier cycle, let us suppose near $M_I = 0.597$ and $\omega_o t = 10°$, are captured, as shown in Fig. 14(a). The fifth channel in Fig. 14(a) triggers the waveform at $\omega_o t = 10°$ while operating at $M_I = 0.597$. The phase currents are captured in no-load to show the ripple presence clearly. After capturing the carrier-cycle four-phase current waveforms ($i_a$, $i_b$, $i_{a'}$, $i_{b'}$) in. csv file from the scope, one can find other two phase currents, $i_c$ and $i_{c'}$, as $i_c = -i_a - i_b$ and $i_{c'} = -i_{a'} - i_{b'}$, as described earlier. The simulated four phase currents for the same $\vec{m}_{\alpha\beta}$ are shown in Fig. 14(d).

One can subtract the carrier-cycle average from the phase current waveforms to get the per-phase ripple current over a carrier cycle, as shown as follows.

$$\tilde{i}_x = i_x - \bar{i}_x; \qquad x = a, b, c, a', b', c'. \tag{13}$$

Here, $i_x$, $\bar{i}_x$, and $\tilde{i}_x$ are the instantaneous current, average current over the carrier cycle, and ripple current of $x$ phase, respectively. The carrier-cycle average of $\bar{i}_x, x = a, b, c, a', b', c'$, is found numerically in MATLAB from the. csv file and is subtracted from the instantaneous phase current, $i_x$, to obtain the ripple currents of six phases. The ripple currents of the four phases at $M_I = 0.597$ and $\omega_o t = 10°$, as obtained from the experimental results, are shown in Fig. 14(b). A similar exercise is also performed in simulation, and Fig. 14(e) shows the simulated carrier-cycle ripple currents at $M_I = 0.597$ and $\omega_o t = 10°$. The ripple currents in $\alpha - \beta$ and $z_1 - z_2$ subspaces can be determined after applying $T$, (1), on the phase ripple currents. Fig. 14(c) and (f) compares the experimental and simulated ripple currents, respectively, in the four subspaces.

Observe that the captured experimental phase current waveforms of Fig. 14(a) contain high-frequency noise at the instants of switching of the six-phase inverter. Note that though switching at any instant happens in one of the six legs, the noise is observed in all line current waveforms. These noises captured by the probe are not part of the current ripple. And these measurement noises also appear in the experimental per-phase ripple currents, Fig. 14(b), or ripple currents in $\alpha - \beta$ and $z_1 - z_2$ subspaces, Fig. 14(c). But, simulated phase currents and the ripple currents are devoid of these high-frequency noises, Fig. 14(d)–(f). Except for these noises, there is a good agreement between the experimental and simulated per-phase ripple current [compare Fig. 14(b) and (e)] and ripple currents in $\alpha - \beta$ and $z_1 - z_2$ subspaces (compare Fig. 14(c) and (f)).

The improvement of the ripple current RMS over the line cycle in OVM by the proposed strategy compared to two existing techniques is first validated through simulation for $\gamma = 2, 6, 10$ with $M_I$ in the range of 0.577 to 0.622. The simulated data points are shown in Fig. 7 by the asterisk marks on top of the analytical plots. The closeness between the analytical plots and the simulated data points confirms the same percentage improvements as in Table V.

Fig. 15 compares $\alpha - \beta$, $z_1 - z_2$, and total ripple current RMS values over the line cycle of the proposed method with the two existing methods as function of $M_I$ for $\gamma = 1.69$. The experimental results' line-cycle ripple current RMS values are calculated considering frequency components in discrete Fourier transform from 1 to 150 kHz to neglect the effect of very high-frequency switching noises, as discussed above. The frequency components of the switching noises are much higher, and thus, it will not impact the ripple calculation, [4]. Generally, the frequencies up to ten times the switching frequency contribute to the current ripple. As the switching frequency in the experiment is 5 kHz, consideration of frequency components up to 150 kHz is

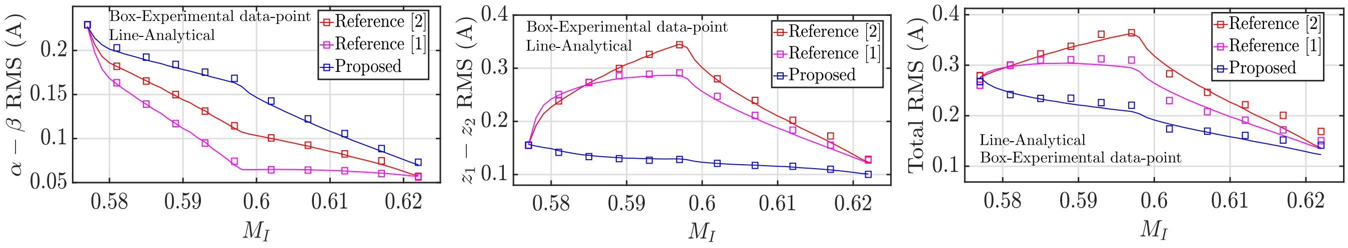

(a) (b) (c)

Fig. 15. Experimental comparisons of $\alpha-\beta$, $z_1-z_2$, and total ripple RMS currents of the proposed technique to the existing techniques at $\gamma = 1.69$. (a) $\alpha-\beta$ RMS Current versus $M_I$. (b) $z_1-z_2$ RMS Current versus $M_I$. (c) Total RMS Current versus $M_I$.

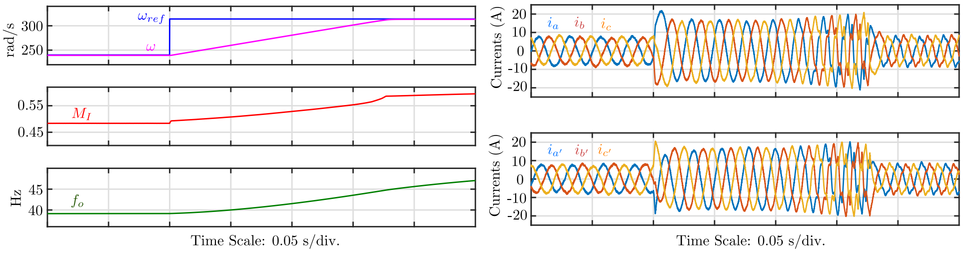

(a) (b)

Fig. 16. Simulated response of RFOC-controlled ASPM for a step change in speed reference. (a) $\omega_{\text{ref}}$, $\omega$, $M_I$, and $f_o$ during speed transient. (b) Six phase currents during speed transient.

sufficient to account for the current ripple RMS. Fig. 15 mentions the absolute RMS currents and the base current for this operation is $\frac{V_{\text{DC}}T_{\text{sw}}}{L_{\alpha\beta}} = \frac{275\times 200e-6}{4e-3} = 13.75$ A. The line plots and the square boxes in Fig. 15 represent the analytical RMS currents and experimentally obtained RMS currents, respectively. Although the RMS ripple currents of [2] and [1] are better in $\alpha-\beta$ plane, the proposed technique has superior ripple performance in $z_1-z_2$ plane, as can be seen from Fig. 15(a) and (b). In terms of total ripple RMS currents, after accounting both the subspace's contributions, the proposed strategy outperforms the existing techniques, as shown in Fig. 15(c). The maximum improvements shown by the proposed strategy compared to the methods of [2] and [1] are 193.89% and 113.02%, respectively. Both of them occur at $M_I = 0.597$. The closeness between analytical plots and the experimental data points verifies the efficacy of the proposed strategy.

## C. Verification of the Dynamic Operation

As the $\alpha-\beta$ plane is the only plane associated with the electromagnetic energy transfer and the torque production of ASPM, the output of ASPM drive will be the reference voltage vector in $\alpha-\beta$ plane, i.e., $m_\alpha$ and $m_\beta$. Using this $\vec{m}_{\alpha\beta}$ the proposed modulation strategy identifies the optimal sequence from the algorithm given in Fig. 6 and applies it on a cycle-by-cycle basis. Hence, the proposed technique can be applied for any scalar or vector control of ASPM. The dynamic operation with the proposed modulation scheme is verified with rotor-flux-oriented-control (RFOC) in simulation. Fig. 16 shows the response of a RFOC-based ASPM drive for a step change in reference speed from 240 rd/s (2292 RPM) to 314 rd/s (2999 RPM) under the constant load torque of 12 N-m. The corresponding changes in modulation index ($M_I$) and output frequency ($f_o$) are shown in Fig. 16(a). It can be seen that the $(M_I, f_o)$ pair is changed from (0.484, 39.14 Hz) to (0.589, 47.04 Hz) during the transient process in 0.175 s. Therefore, the ASPM moves from linear region ($M_I \leq 0.577$) to OVM region ($M_I > 0.577$). The corresponding six-phase currents are shown in Fig. 16(b).

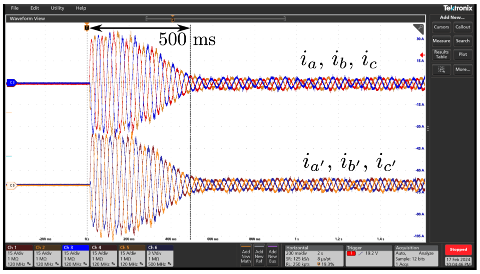

Current Scale: 15A/div. Time Scale: 200ms/div.

Fig. 17. Experimental result to show the start-up of ASPM under V/f control.

Fig. 17 shows the experimental six phase currents of ASPM during start-up under V/f control. The starting $M_I$ and $f_o$ are kept at 0.2 and 16 Hz, respectively. The initial rate of change of $(M_I, f_o)$ pair is chosen as (0.04, 3.2 Hz) per second so that the initial start-up transient current never exceeds two times its full-load rated current. The ASPM has the following specifications- 5 kW, 115 V RMS in six-phase configuration, efficiency 86%, power factor 0.85. Hence, the peak value of the rated current per phase is $\frac{\sqrt{2}\times 5000}{6\times 115\times 0.86\times 0.85} = 14$ A. As seen from Fig. 17, the maximum peak value of the six-phase current is 30 A, close to two times the rated peak current, and the initial start-up transient is over within 0.5 s. The six phase currents remain balanced under both transient and steady-state operation. Note that the ASPM has not reached its rated speed or full load within the time interval for which the waveforms are captured in Fig. 17.

## VI. CONCLUSION

This article studies the high-frequency current ripple performances of the OVM techniques of ASPM, which apply the minimum low-frequency RMS voltage in the harmonic subspace, i.e., $z_1 - z_2$ plane. For ripple current study, the paper considers all possible switching sequences in the OVM region of ASPM with the following two properties– 1) none of the semiconductor devices switches more than once within a carrier cycle; 2) the sequences are mirror-symmetric along the half-carrier period. The resulting sequences can be grouped as four sequence groups for one part of the OVM region, named OVMZ1, and two in the remaining part, known as OVMZ2. Compared to linear techniques, the ripple analysis of OVM techniques need to consider the nonzero average voltage in $z_1 - z_2$ plane. This current-ripple is a function of the PWM sequence, the position of the reference voltage vector in the OVM region of the energy-transferring plane, $\alpha - \beta$, and a machine parameter, $\gamma$, which is the ratio of high-frequency equivalent circuit inductances in $\alpha - \beta$ and $z_1 - z_2$. This article finds the sequences with minimum current ripple in both OVMZ1 and OVMZ2. Two sequence groups in OVMZ1 have two redundant states. The dwell time distribution between these redundant states impacts the current ripple, which is also studied in the paper. The article shows that two sequences in OVMZ1 and one in OVMZ2 give the minimum current ripple for the feasible range of $\gamma$ ($1.5 \leq \gamma \leq 10$). Subsequently, it proposes an optimal technique combining the above sequences that shows 623.67% and 416.53% improvements in the OVM region at $\gamma = 10$ compared to two existing methods in the literature. The efficacy of the proposed technique is verified through simulation and experiments on a hardware prototype at a maximum power of 4.2 kW.

## APPENDIX

## EXAMPLE OF EFFICIENCY IMPROVEMENT IN MEDIUM-VOLTAGE HIGH-POWER MACHINE

Let’s consider a 110 kW, 2 kV, 50 Hz, 600 RPM, 3$\phi$ induction motor, B.S.S. 168-1936 machine, whose design is given in [33]. This machine can be driven with $V_{DC}$ =1.5 kV in ASPM configuration. From the given design in [33], the approximate equivalent parameters in 6$\phi$ configuration are deducted, which are as follows- $r_s = 0.675\ \Omega$, $L_{\alpha\beta} = 4.23$ mH. Let the $\gamma$ of the machine is 10 and $F_{sw}$ of this high-power drive is limited to 1.5 kHz. Therefore, the base current, $\frac{V_{DC}T_{sw}}{L_{\alpha\beta}}$, is 236.41 A. The performance at $\gamma = 10$ is given in Fig. 7(i), from where the ripple currents and the associated copper loss can be calculated. The copper losses incurred due to proposed method and the techniques of [1] and [2] are 684.5 W, 3424.9 W, and 5023.8 W, respectively, at $M_I = 0.597$. Hence, the proposed technique improves the efficiency approximately by 2.5% and 3.94% compared to the existing techniques.

## ACKNOWLEDGMENT

The authors would like to thank Naresh Rana and Prosen Dey for their support and assistance provided to take some of the experimental results.

## REFERENCES

[1] C. Zhou, G. Yang, and J. Su, “Pwm strategy with minimum harmonic distortion for dual three-phase permanent-magnet synchronous motor drives operating in the overmodulation region,” *IEEE Trans. Power Electron.*, vol. 31, no. 2, pp. 1367–1380, Feb. 2016.

[2] S. Paul and K. Basu, “Overmodulation techniques of asymmetrical six-phase machine with optimum harmonic voltage injection,” *IEEE Trans. Ind. Electron.*, vol. 68, no. 6, pp. 4679–4690, Jun. 2021, doi: 10.1109/TIE.2020.2989709.

[3] M. J. Duran and F. Barrero, “Recent advances in the design, modeling, and control of multiphase machines–Part II,” *IEEE Trans. Ind. Electron.*, vol. 63, no. 1, pp. 459–468, Jan. 2016.

[4] S. Paul and K. Basu, “Linear PWM techniques of asymmetrical six-phase machine with optimal current ripple performance,” *IEEE Trans. Ind. Electron.*, vol. 70, no. 2, pp. 1298–1309, Feb. 2023, doi: 10.1109/TIE.2022.3156161.

[5] W. Tahaa, P. Azerb, A. D. Callegaro, and A. Emadi, “Multiphase traction inverters: State-of-the-art review and future trends,” *IEEE Access*, vol. 10, pp. 4580–4599, 2022.

[6] F. Barrero and M. J. Duran, “Recent advances in the design, modeling, and control of multiphase machines–Part I,” *IEEE Trans. Ind. Electron.*, vol. 63, no. 1, pp. 449–458, Jan. 2016.

[7] A. Salem and M. Narimani, “A review on multiphase drives for automotive traction applications,” *IEEE Trans. Transport. Electrific.*, vol. 5, no. 4, pp. 1329–1348, Dec. 2019.

[8] H. S. Che, M. J. Duran, E. Levi, M. Jones, W.-P. Hew, and N. A. Rahim, “Postfault operation of an asymmetrical six-phase induction machine with single and two isolated neutral points,” *IEEE Trans. Power Electron.*, vol. 29, no. 10, pp. 5406–5416, Oct. 2014, doi: 10.1109/TPEL.2013.2293195.

[9] D. Keller, M. Kuenzler, A. Karayel, Q. Werner, and N. Parspour, “Potential of dual three-phase PMSM in high performance automotive powertrains,” in *Proc. Int. Conf. Elect. Mach.*, 2020, vol. 1, pp. 1800–1806, doi: 10.1109/ICEM49940.2020.9270907.

[10] W. N. W. A. Munim, M. J. Duran, H. S. Che, M. Bermúdez, I. González-Prieto, and N. A. Rahim, “A unified analysis of the fault tolerance capability in six-phase induction motor drives,” *IEEE Trans. Power Electron.*, vol. 32, no. 10, pp. 7824–7836, Oct. 2017.

[11] Y. Zhao and T. A. Lipo, “Space vector PWM control of dual three-phase induction machine using vector space decomposition,” *IEEE Trans. Ind. Appl.*, vol. 31, no. 5, pp. 1100–1109, Sep./Oct. 1995.

[12] D. Hadiouche, L. Baghli, and A. Rezzoug, “Space-vector PWM techniques for dual three-phase AC machine: Analysis, performance evaluation, and DSP implementation,” *IEEE Trans. Ind. Appl.*, vol. 42, no. 4, pp. 1112–1122, Jul./Aug. 2006.

[13] K. Marouani, L. Baghli, D. Hadiouche, A. Kheloui, and A. Rezzoug, “A new PWM strategy based on a 24-sector vector space decomposition for a six-phase VSI-fed dual stator induction motor,” *IEEE Trans. Ind. Electron.*, vol. 55, no. 5, pp. 1910–1920, May 2008.

[14] S. Paul and K. Basu, “A new space-vector PWM technique of two-level inverter fed asymmetrical six-phase machine: Analysis and performance evaluation,” in *Proc. IEEE Energy Convers. Congr. Expo.*, 2021, pp. 4796–4802, doi: 10.1109/ECCE47101.2021.9595332.

[15] K. Cui, C. Wang, M. Zhou, and S. Sun, “Comprehensive investigation of space-vector PWM including novel switching sequences for dual three-phase motor drives,” *IEEE Trans. Transport. Electrific.*, vol. 9, no. 1, pp. 1350–1362, Mar. 2023.

[16] L. Gopi and G. Narayanan, “Advanced 24-sector bus-clamping PWM techniques for dual inverter-fed split-phase induction motor drives,” in *Proc. IEEE Int. Conf. Power Electron., Smart Grid, Renewable Energy*, 2022, pp. 1–6.

[17] M. S. Shaikh et al., “Performance investigation on SVPWM sequences based on reduced common-mode voltage in dual three-phase asymmetrical machine,” *IEEE Trans. Energy Convers.*, vol. 36, no. 4, pp. 2884–2893, Dec. 2021.

[18] D. Ye et al., “Variable switching sequence PWM strategy of dual three-phase machine drive for high-frequency current harmonic suppression,” *IEEE Trans. Power Electron.*, vol. 35, no. 5, pp. 4984–4995, May 2020.

[19] L. Gopi and G. Narayanan, “Per-phase analysis, efficient implementation and performance evaluation of a 24-sector discontinuous PWM for split-phase induction motor drives,” *IEEE Trans. Ind. Appl.*, vol. 59, no. 1, pp. 897–909, Jan./Feb. 2023.

[20] S. Paul and K. Basu, “A three-phase inverter based overmodulation strategy of asymmetrical six-phase induction machine,” *IEEE Trans. Power Electron.*, vol. 36, no. 5, pp. 5802–5817, May 2021, doi: 10.1109/TPEL.2020.3026816.

[21] K. Gopakumar, V. Ranganthan, and S. Bhat, “Split-phase induction motor operation from PWM voltage source inverter,” *IEEE Trans. Ind. Appl.*, vol. 29, no. 5, pp. 927–932, Sep./Oct. 1993.

[22] A. G. Yepes and J. Doval-Gandoy, “Simple carrier-based PWM for prolonged high DC-link utilization for symmetrical and asymmetrical $n$-phase AC drives,” *IEEE Trans. Power Electron.*, vol. 36, no. 8, pp. 8696–8712, Aug. 2021.

[23] D. Yazdani, S. A. Khajehoddin, A. Bakhshai, and G. Joos, “Full utilization of the inverter in split-phase drives by means of a dual three-phase space vector classification algorithm,” *IEEE Trans. Ind. Electron.*, vol. 56, no. 1, pp. 120–129, Jan. 2009.

[24] L. Wu, J. Li, Y. Lu, and K. He, “Strategy of synchronized SVPWM for dual three-phase machines in full modulation range,” *IEEE Trans. Power Electron.*, vol. 37, no. 3, pp. 3272–3282, Mar. 2022.

[25] A. M. Hava, R. J. Kerkman, and T. A. Lipo, “Simple analytical and graphical methods for carrier-based PWM-VSI Drives,” *IEEE Trans. Power Electron.*, vol. 14, no. 1, pp. 49–61, Jan. 1999.

[26] D. G. Holmes, “The significance of zero space vector placement for carrier-based PWM schemes,” *IEEE Trans. Ind. Appl.*, vol. 32, no. 5, pp. 1122–1129, Sep./Oct. 1996.

[27] D. G. Holmes and T. A. Lipo, *Pulse Width Modulation for Power Converters: Principles and Practice*, vol. 18. Hoboken, NJ, USA: Wiley, 2003.

[28] D. Hadiouche, H. Razik, and A. Rezzoug, “On the modeling and design of dual-stator windings to minimize circulating harmonic currents for VSI fed AC machines,” *IEEE Trans. Ind. Appl.*, vol. 40, no. 2, pp. 506–515, Mar./Apr. 2004.

[29] M. S. Shaikh and R. Maurya, “Simplified implementation of SVPWM techniques for a six-phase machine with reduced current distortion features,” *IET Electric Power Appl.*, vol. 13, no. 11, pp. 1753–1762, 2019.

[30] D. Zhao, V. S. S. P. K. Hari, G. Narayanan, and R. Ayyanar, “Space-vector-based hybrid pulsewidth modulation techniques for reduced harmonic distortion and switching loss,” *IEEE Trans. Power Electron.*, vol. 25, no. 3, pp. 760–774, Mar. 2010, doi: 10.1109/TPEL.2009.2030200.

[31] L. Gopi and G. Narayanan, “Four-dimensional 24-sector SVPWM techniques for split-phase induction motor drives: Analysis of modulation process and efficient implementation,” in *Proc. IEEE Int. Conf. Power Electron., Smart Grid, Renewable Energy*, 2022, pp. 1–6.

[32] S. Paul and K. Basu, “A carrier-comparison-based implementation strategy of a 24-sector-based SVPWM technique of asymmetrical six-phase machine in overmodulation region,” in *Proc. IECON 48th Annu. Conf. IEEE Ind. Electron. Soc.*, 2022, pp. 1–7, doi: 10.1109/IECON49645.2022.9968355.

[33] M. Say, *The Performance and Design of Alternating Current Machines: Transformers, Three-phase Induction Motors and Synchronous Machines*, PITMAN, 1948. [Online]. Available: https://books.google.com/books?id=NQNPAAAAMAAJ

**Sayan Paul** (Member, IEEE) received the B.Tech. degree from the National Institute of Technology, Durgapur, India, in 2014, the M.Sc. (Engg.) degree from the Indian Institute of Science, Bangalore, India, in 2018, in electrical engineering, and the Ph.D. degree in electrical engineering from the Indian Institute of Science, Bangalore, India, in 2024.

He is currently a Postdoctoral Researcher with the University of Colorado Boulder. His research interests include PWM techniques, modeling and controlling multiphase drives and multilevel converters, high-frequency switched dc-to-dc and ac-to-dc power converters, etc.

Dr. Paul was a recipient of “The Hay Medal” (Gold Medal for the year 2019-20) by the Indian Institute of Science, Bangalore, for the best M.Sc.(Engg.) thesis, he also received “The Murthy Govindaraju Research Endowment Award in Power Electronics” in 2023, and “Prof. Joseph Vithayathil Travel Award” in 2022 from the Indian Institute of Science, Bangalore.

**Kaushik Basu** (Senior Member, IEEE) received the B.E. degree from the Bengal Engineering and Science University, Shibpore, India, in 2003, the M.Sc. degree in electrical engineering from the Indian Institute of Science (IISc), Bangalore, India, in 2005, and the Ph.D. degree in electrical engineering from the University of Minnesota, Minneapolis, MN, USA, in 2012, respectively.

His Ph.D. advisor was late Prof. Ned Mohan. He was a Design Engineer with Cold Watt India in 2006 and an Electronics and Control Engineer with Dynapower Corporation USA from 2013 to 2015. He is an Associate Professor with the Department of Electrical Engineering at the IISc. His research interests include most aspects of Power Electronic converter design from a few kW to a few MW for applications ranging from space, grid integration of renewables and storage to fast charging of electric vehicles.

Dr. Basu served as the Technical Program Committee Vice-Chair of IEEE ECCE 2020 and 2022. In 2019, he received the Prof. Priti Shankar Teaching Award from IISc. He has coauthored more than 100 papers in peer reviewed journals and conferences. As a co-author, he received the Second Best Prize Paper Award from IEEE TRANSACTIONS ON TRANSPORTATION ELECTRIFICATION in 2021. He is the founding chair of both IEEE PELS and IES Bangalore Chapter. He is an Associate Editor of IEEE TRANSACTIONS ON POWER ELECTRONICS AND IEEE TRANSACTIONS ON INDUSTRIAL ELECTRONICS. He did serve as an AE of Springer Journal of Power Electronics, 2022-24. He is currently a Regional (R10) Distinguished Lecturer of IEEE PELS.